MACHINE LEARNING MEMORY KERNELS AS CLOSURE FOR NON-MARKOVIAN STOCHASTIC PROCESSES

Antonio Russo
Department of Chemical Engineering
Imperial College London
London SW7 2AZ, UK

Miguel A. Durán-Olivencia
Department of Chemical Engineering
Imperial College London
London SW7 2AZ, UK

Ioannis G. Kevrekidis
Department of Chemical and Biomolecular Engineering
Johns Hopkins University
Baltimore MD 21218, USA

Serafim Kalliadasis
Department of Chemical Engineering
Imperial College London
London SW7 2AZ, UK

ABSTRACT

Finding the dynamical law of observable quantities lies at the core of physics. Within the particular field of statistical mechanics, the generalized Langevin equation (GLE) comprises a general model for the evolution of observables covering a great deal of physical systems with many degrees of freedom and an inherently stochastic nature. Although formally exact, the GLE brings its own great challenges. It depends on the complete history of the observables under scrutiny, as well as the microscopic degrees of freedom, all of which are often inaccessible. We show that these drawbacks can be overcome by adopting elements of machine learning from empirical data, in particular coupling a multilayer perceptron (MLP) with the formal structure of the GLE and calibrating the MLP with the data. This yields a powerful computational tool capable of describing noisy complex systems beyond the realms of statistical mechanics. It is exemplified with a number of representative examples from different fields: from a single colloidal particle and particle chains in a thermal bath to climatology and finance, showing in all cases excellent agreement with the actual observable dynamics. The new framework offers an alternative perspective for the study of non-equilibrium processes opening also a new route for stochastic modelling.

1 Introduction

The mathematical description of both natural and technological processes requires governing equations for the observed temporal evolution of pertinent process properties. Such quantities can often be directly measured, and act as a bridge between theory and experiments. Consequently, they are known as *observables*. Physical systems can be analyzed following either a microscopic description, i.e. a complete description of each component in the system, or a macroscopic approach, i.e studying the system as a whole. The set of observables, $\boldsymbol{\mathcal{O}} = \{\mathcal{O}_i\}_{i=1,2,\ldots}$, which uniquely describes the macroscopic state of a system is typically termed as *canonical observables*, e.g. pressure and temperature to describe a thermodynamic state. At the same time, the minimum set of variables, $\mathbf{z} = \{z_j\}_{j=1,2,\ldots}$, required to describe the microscopic state of a dynamical system is referred to as *degrees of freedom* (DoF). Statistical mechanics deals with the connection between macroscopic observables (or simply observables) and DoF. From a purely theoretical point of view, any observable can be understood as a function of the system's DoF, i.e. $\mathcal{O}_i = f_i(\mathbf{z})$. Given the huge number of DoF a physical system typically involves, finding the exact functional form f which connects the given observable and the system's DoF represents an overwhelming challenge. It is formally possible to go from the DoF description of the system (e.g. from Newton's equations of motion) to one in terms of observables via dimensionality reduction which retains the main effects at the observables' level and allows us to describe the same phenomenon with a substantially reduced number of variables. Such a reduction has the convenience of a simpler representation of the system, enabling also its study in a computationally inexpensive manner. This is of central importance for

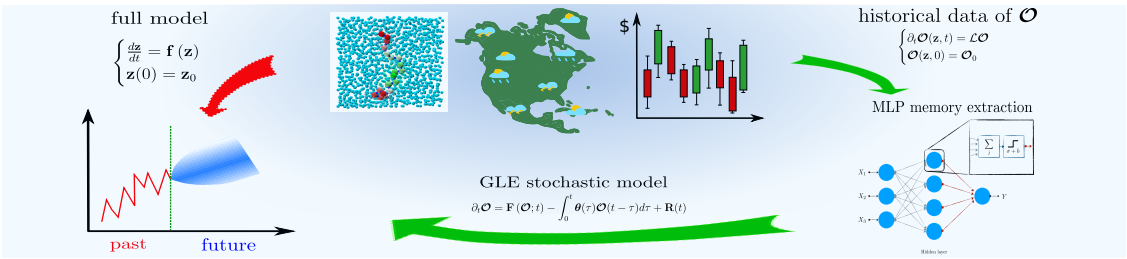

Figure 1: Two possible approaches to simulate the time evolution of dynamical-systems' observable. As a first approach, the full deterministic dynamical system (red arrow) is solved. Despite the advantage of being exact, this approach is often not suitable either because is computationally prohibitive or because a model of the full DoF system is not accessible. An alternative consists of building a GLE model for the observable and parameterizing it through a multilayer perceptron, given appropriate historical data (green arrows). Suitable system observables can be selected based either on prior knowledge of the system or directly on historical data by means of techniques such as principal-component analysis, auto-encoders and diffusion maps[36, 11].

the understanding of complex systems, given the huge computational cost required to integrate the DoF over time in realistic scenarios. Indeed, the number of DoF is typically as large as Avogadro's number ($N_{\mathrm{A}} \sim 10^{23}$). Unfortunately, postulating a dynamical law for an observable is in general non-trivial. This necessitates the quest for finding the connection between the DoF and the observable dynamics.

There exists a mathematical formalism which allows us to get the formal structure of the equations describing the observable dynamics starting from the deterministic DoF's time-evolution equations without knowing exactly the functional dependency of the observables on the DoF. This dimensionality-reduction formalism is known as the "projection-operator (PO) technique", and was originally introduced by Mori and Zwanzig[32, 41] and comprehensive analysis of the formalism in Ref.[7] where reduction techniques are reviewed. Despite not yielding closed governing equations (precisely because of the inherent limitation of not knowing the functional relationship f between the observables and the DoF), it produces a relatively simple and versatile model after some convenient simplifications. The first success of the PO formalism was the derivation of the Brownian dynamics, for which only a phenomenological derivation by Langevin was available at the time[28].

1.1 Mori-Zwanzig's formalism

Let us consider the following (linear of non-linear) deterministic dynamical system:

$$\begin{cases} \frac{d\mathbf{z}}{dt} = \mathbf{f}(\mathbf{z}) \\ \mathbf{z}(0) = \mathbf{z}_0 \end{cases} \tag{1}$$

where $\mathbf{z} \in \mathbb{R}^n$ is a vector of independent variables. For the system in Eq. (1), it can be defined a set of observables $\mathcal{O}(\mathbf{z},t) = \phi(\mathbf{z}(t))$, where ϕ represent the transformation map between $\mathbf{z}$ and $\mathcal{O}$. By using the chain rule, it is easy to show that the evolution equation of $\mathcal{O}(\mathbf{z},t)$ can be written as:

$$\begin{cases} \frac{\partial \mathcal{O}}{\partial t}(\mathbf{z},t) = \mathcal{L}\mathcal{O} \\ \mathcal{O}(\mathbf{z},0) = \mathcal{O}_0 \end{cases} \tag{2}$$

where it was introduced the operator $\mathcal{L} = \mathbf{f}(\mathbf{z}) \cdot \nabla_{\mathbf{z}}$. It follows that the solution of Eq. (2) can be written as:

$$\mathcal{O}(\mathbf{z},t) = e^{\mathcal{L}t}\mathcal{O}_0 \tag{3}$$

where the exponential has to be intended as the power series that defines the exponential map between matrices.

If we are only interested in the dynamics of some observables $\mathcal{O}$, rather then the whole solution $\mathbf{z}(t)$, we can define a projection operator $\mathcal{P}$, which maps functions of $\mathbf{z}$ into function of $\mathcal{O}$. It is worth underlining that, in general, the set of observables $\mathcal{O}$ may be defined by a linear or nonlinear transformation of $\mathbf{z}$, but in any case the evolution of $\mathcal{O}$ is supposed to be unitary, i.e. $\mid \mathcal{O}(t) \mid^2 = \mid \mathcal{O}(0) \mid^2$. A simple, but still important, scenario is given by $\mathcal{O}$ being a subset of $\mathbf{z}$. As we will see later, this case plays a fundamental role in dimensional reductions of multi-component systems, i.e. colloidal particles in a thermal bath. Given a projection operator $\mathcal{P}$, namely a transformation from a vector space to itself such that $\mathcal{P}^2 = \mathcal{P}$, one can follow Mori-Zwanzig's formalism [40, 32, 41] to obtain a form of Eq. (2) suitable for system dimensionality reduction. Note that at this point no constrain is put on the form of the projection operator. After

defining the operator $\mathcal{Q} = \mathbf{1} - \mathcal{P}$, orthogonal to $\mathcal{P}$, Eq. (2) can be rewritten as:

$$\frac{\partial \boldsymbol{\mathcal{O}}}{\partial t}(\mathbf{z}, t) = \mathcal{L} e^{\mathcal{L}t} \boldsymbol{\mathcal{O}}_0 = e^{\mathcal{L}t} \mathcal{P}\mathcal{L}\boldsymbol{\mathcal{O}}_0 + e^{\mathcal{L}t} \mathcal{Q}\mathcal{L}\boldsymbol{\mathcal{O}}_0 \tag{4}$$

Duhamel-Dyson's formula allows to rewrite the exponential term $e^{\mathcal{L}t}$ as:

$$e^{\mathcal{L}t} = e^{\mathcal{Q}t} + \int_0^t e^{\mathcal{L}(t-\tau)}\, \mathcal{P}\, e^{\mathcal{Q}\tau}\, d\tau \tag{5}$$

and, consequently, Eq. (4) becomes the so called Mori-Zwanzig's equation:

$$\begin{aligned} \frac{\partial \boldsymbol{\mathcal{O}}}{\partial t}(\mathbf{z}, t) =& e^{\mathcal{L}t} \mathcal{P}\mathcal{L}\boldsymbol{\mathcal{O}}_0 + \\ & \int_0^t e^{\mathcal{L}(t-\tau)} \mathcal{P}\mathcal{L} e^{\mathcal{Q}\tau} \mathcal{Q}\mathcal{L}\boldsymbol{\mathcal{O}}_0\, d\tau + e^{\mathcal{Q}\mathcal{L}t} \mathcal{Q}\mathcal{L}\boldsymbol{\mathcal{O}}_0 \end{aligned} \tag{6}$$

The first term is the Markovian contribution, the second constitutes the memory term and the last one is often interpreted as the noise. It is worth noticing that, at this stage, Eq. (6) is exactly equivalent to Eq. (1) and is valid independently from the specific choice of the projection operator $\mathcal{P}$. Mori and Zwanzig [32, 41, 42] proposed two different projection operators leading to different forms of GLE, that we will briefly discuss in next sections.

If we name the noise term $\mathbf{R}(t) = e^{\mathcal{Q}\mathcal{L}t} \mathcal{Q}\mathcal{L}\boldsymbol{\mathcal{O}}_0$, then the following dynamical system remains determined:

$$\begin{cases} \dfrac{\partial \mathbf{R}}{\partial t}(\boldsymbol{\mathcal{O}}_0, t) = \mathcal{Q}\mathcal{L}\mathbf{R}(\boldsymbol{\mathcal{O}}_0, t), \\ \mathbf{R}(\boldsymbol{\mathcal{O}}_0, t) = \mathcal{Q}\mathcal{L}\boldsymbol{\mathcal{O}}_0. \end{cases} \tag{7}$$

Projecting Eq. (7) according to $\mathcal{P}$, it follows:

$$\begin{cases} \mathcal{P}\dfrac{\partial \mathbf{R}}{\partial t}(\boldsymbol{\mathcal{O}}_0, t) = \mathcal{P}\mathcal{Q}\mathcal{L}\mathbf{R}(\boldsymbol{\mathcal{O}}_0, t) = \mathbf{0}, \\ \mathcal{P}\mathbf{R}(\boldsymbol{\mathcal{O}}_0, t) = \mathcal{P}\mathcal{Q}\mathcal{L}\boldsymbol{\mathcal{O}}_0 = \mathbf{0}, \end{cases} \tag{8}$$

where we have used the property of the projection operator $\mathcal{P}\mathcal{Q} = \mathbf{0}$. This shows that $\mathbf{R}(t)$ is orthogonal to the range of $\mathcal{P}$ at any time t. However, in order to express $\mathbf{R}(t)$ as a stochastic process, it is necessary to have either time scale separation or weak coupling between resolved and unresolved variables [13]. When at least one of such conditions occurs, at least asymptotically, the influence of the unresolved variables may be interpreted as sum of many uncorrelated events, and consequently can be treated with Central Limit Theorem [15]. Thus, it is the Central Limit Theorem that determines the Gaussian shape for the distribution of $\mathbf{R}(t)$, while its time correlation follows from the fluctuation dissipation theorem, as shown in what follows.

Mori's projection operator The projection operator introduced by Mori [32], when applied to a general variable $\mathbf{A}(\mathbf{z})$, is defined as:

$$\mathcal{P}\mathbf{A}(\mathbf{z}) = \langle \mathbf{A}, \boldsymbol{\mathcal{O}}_0 \rangle \langle \boldsymbol{\mathcal{O}}_0, \boldsymbol{\mathcal{O}}_0 \rangle^{-1} \boldsymbol{\mathcal{O}}_0 \tag{9}$$

where the inner product $\langle \mathbf{A}, \mathbf{B} \rangle$ is defined as

$$\langle \mathbf{A}, \mathbf{B} \rangle = \int \rho(\mathbf{z}) \mathbf{A}(\mathbf{z}) \mathbf{B}^*(\mathbf{z})\, d\mathbf{z} \tag{10}$$

with $\rho(\mathbf{z})$ being a normalized probability density function defined in the phase space of the original system and $\mathbf{B}^*$ the conjugate transpose of $\mathbf{B}$. In case of systems with Hamiltonian $\mathcal{H}$ in a canonical ensemble, the probability density function is $\rho(\mathbf{z}) = Z^{-1} e^{-\beta \mathcal{H}(\mathbf{z})}$, where Z is the partition function and $\beta = k_B T$. Employing Mori's operator in Eq. (6), we obtain the Markovian term:

$$e^{\mathcal{L}t} \mathcal{P}\mathcal{L}\boldsymbol{\mathcal{O}}_0 = \langle \mathcal{L}\boldsymbol{\mathcal{O}}_0, \boldsymbol{\mathcal{O}}_0 \rangle \langle \boldsymbol{\mathcal{O}}_0, \boldsymbol{\mathcal{O}}_0 \rangle^{-1} \boldsymbol{\mathcal{O}}(t). \tag{11}$$

Moreover, from the definition of $\mathbf{R}(t)$, we obtain the memory term:

$$\int_0^t e^{\mathcal{L}(t-\tau)} \mathcal{P}\mathcal{L} e^{\mathcal{Q}\tau} \mathcal{Q}\mathcal{L}\boldsymbol{\mathcal{O}}_0\, d\tau = -\int_0^t \boldsymbol{\theta}(\tau) \boldsymbol{\mathcal{O}}(t-\tau)\, d\tau \tag{12}$$

where the memory kernel is defined as $\boldsymbol{\theta}(t) = -\langle \mathcal{L}\mathbf{R}(t), \boldsymbol{\mathcal{O}}_0 \rangle \langle \boldsymbol{\mathcal{O}}_0, \boldsymbol{\mathcal{O}}_0 \rangle^{-1}$. Since $\mathcal{Q}\mathbf{R}(t) = \mathbf{R}(t)$, and $\mathcal{L}$ is an anti-Hermitian operator [42], it follows that $\langle \mathcal{L}\mathbf{R}(t), \boldsymbol{\mathcal{O}}_0 \rangle = -\langle \mathbf{R}(t), \mathcal{L}\boldsymbol{\mathcal{O}}_0 \rangle = -\langle \mathbf{R}(t), \mathcal{Q}\mathcal{L}\boldsymbol{\mathcal{O}}_0 \rangle = -\langle \mathbf{R}(t), \mathbf{R}(0) \rangle$. Hence, we obtain the following relation:

$$\boldsymbol{\theta}(t) = \langle \mathbf{R}(t), \mathbf{R}(0) \rangle \langle \boldsymbol{\mathcal{O}}_0, \boldsymbol{\mathcal{O}}_0 \rangle^{-1}, \tag{13}$$

which constitutes the fluctuation dissipation theorem.

Zwanzig projection operator As Zwanzig pointed out, Mori's projection operator leads to a linearised GLE [42]. Zwanzig [40, 42] defined the projection operator applied to the variable $\mathbf{A}(\mathbf{z})$ through the following conditional expectation:

$$\mathcal{P}\mathbf{A}(\mathbf{z}) = \frac{\int \rho(\mathbf{z})\, \mathbf{A}(\mathbf{z})\, \delta(\boldsymbol{\mathcal{O}} - \phi(\mathbf{z}))\, d\mathbf{z}}{\int \rho(\mathbf{z})\, \delta(\boldsymbol{\mathcal{O}} - \phi(\mathbf{z}))\, d\mathbf{z}}, \tag{14}$$

where $\delta(\boldsymbol{\mathcal{O}} - \phi(\mathbf{z})) = \prod_j \delta(\boldsymbol{\mathcal{O}}_j - \phi_j)$. In molecular dynamics, the set of observables is often defined as a subset of the original coordinates, namely $\boldsymbol{\mathcal{O}} \subseteq \mathbf{z}$. In this case, Zwanzig's projection operator allows to express the Markovian term in Eq. (6) as function of the potential of mean force. To show this, let us consider an isothermal Hamiltonian system of N particles with coordinates $\mathbf{z} = \{\mathbf{r}, \mathbf{p}\}$, where $\mathbf{r} = \{\mathbf{r}_1 \dots \mathbf{r}_N\}$ and $\mathbf{p} = \mathbf{p}_1 \dots \mathbf{p}_N$ are position and momenta, respectively. With $\mathbf{f}(\mathbf{z}) = -\nabla_{\mathbf{z}} V(\mathbf{z})$, Eq. (1) gives the Newton's equations of motion for a system of interacting particles. Suppose one is interested in the dynamical evolution of only n of the original N particles, whose coordinates (called relevant variables) and are indicated as $\tilde{\mathbf{z}} = \{\mathbf{r}_1 \dots \mathbf{r}_n, \mathbf{p}_1 \dots \mathbf{p}_n\}$. The remaining variables, called unresolved variables, are denoted by $\hat{\mathbf{z}} = \{\mathbf{r}_{n+1} \dots \mathbf{r}_N, \mathbf{p}_{n+1} \dots \mathbf{p}_N\}$. Hence, inserting Zwanzig's operator in Eq. (6), we obtain the Markovian term in the form:

$$\mathcal{P}\mathcal{L}\tilde{\mathbf{z}} = \frac{\int\, -\nabla_{\mathbf{z}} V(\mathbf{z}) e^{-\beta\mathcal{H}(\mathbf{z})}\, \delta(\mathbf{z} - \tilde{\mathbf{z}})\, d\mathbf{z}}{\int e^{-\beta\mathcal{H}(\mathbf{z})}\, \delta(\mathbf{z} - \tilde{\mathbf{z}})\, d\mathbf{z}} = -\nabla_{\tilde{\mathbf{z}}} V^{\text{PMF}}(\tilde{\mathbf{z}}) \tag{15}$$

where V^{PMF} is known as potential of mean force. Moreover, the memory term can be written in terms of the noise term as:

$$\int_0^t e^{\mathcal{L}(t-\tau)} \mathcal{P}\mathcal{L}\mathbf{R}(\tau)\, d\tau. \tag{16}$$

Ref. [5] has shown that the term in Eq. (16) is null for the position coordinates $\mathbf{r}$, while can expressed for the momentum coordinates $\mathbf{p}$ as the convolution $-\int_0^t \boldsymbol{\theta}(\tau)\mathbf{p}(t-\tau)d\tau$.

Generalized Langevin Equation In short, the PO formalism makes it possible to derive the time-evolution equation for $\boldsymbol{\mathcal{O}}$, which results in a set of first-order generalized Langevin equations (GLEs). The structure of a GLE typically consists of a:

- Markovian (mean-force) term which depends on the instantaneous values of the observables under consideration [23, 17, 5],
- Non-Markovian (so-called memory) time-convolution term which depends on the historical values of the observables at hand. In many cases the Non-Markovian term can be expressed simply as the convolution between the observables and a tensor function (so-called memory kernel), $\boldsymbol{\theta}(t)$, which plays the role of a viscosity kernel [23, 17, 5].
- Noise term which depends on both the observables and all DoF's initial conditions, and which is why it is interpreted as a purely random term.

The PO formalism makes it possible to assert that any set of observables will follow the GLE dynamics:

$$\partial_t \boldsymbol{\mathcal{O}}(t) = \mathbf{F}(\boldsymbol{\mathcal{O}}(t)) - \int_0^t \boldsymbol{\theta}(\tau)\boldsymbol{\mathcal{O}}(t-\tau)d\tau + \mathbf{R}(t). \tag{17}$$

with $\mathbf{F}(\boldsymbol{\mathcal{O}}(t))$ being the deterministic term, and $\mathbf{R}(t)$ the stochastic term orthogonal to $\boldsymbol{\mathcal{O}}$, with correlation given by the fluctuation-dissipation theorem:

$$\langle \mathbf{R}(t), \mathbf{R}(t') \rangle = \boldsymbol{\theta}(t-t') \langle \boldsymbol{\mathcal{O}}, \boldsymbol{\mathcal{O}} \rangle. \tag{18}$$

In Eq. (18) we have used $\langle a, b \rangle = \int d\mathbf{z}\, \rho(\mathbf{z}) a(\mathbf{z}) b^\dagger(\mathbf{z})$ where $\mathbf{z} \in \mathbb{R}^n$ is the system's DoF and $\rho(\mathbf{z})$ a normalized probability density function, and $b^\dagger$ the conjugate transpose of b. As can be readily checked, the non-Markovian term depends on the temporal trace of the system and is characterised by the memory-kernel function $\boldsymbol{\theta}(t)$. This function also determines the noise term $\mathbf{R}(t)$ through the fluctuation-dissipation theorem given above. Therefore, ascertaining the memory kernel is crucial for preserving the main features of the high-dimensional (microscopic) dynamics into the dimensionally-reduced time-evolution equations. Unfortunately, the memory kernel depends on the whole set of DoF and their full history[16] which makes the problem intractable as illustrated in Fig. 1. Because of these difficulties, more often than not, the memory kernel $\boldsymbol{\theta}(t)$ is approximated through the Markovian hypothesis, $\boldsymbol{\theta}(t) = \boldsymbol{\theta}_0 \delta(t)$. However, this approximation as much as it yields drastically simpler LEs, it comes at the expense of accuracy representing considerable source of errors as we will demonstrate.

1.2 Main highlights and applications

Analytical expressions for the memory kernel are only accessible for very specific, and often ideal, systems such as the academic case of a particle in a harmonic-oscillator heat bath [42]. But in the general case it cannot be determined from first principles and analysis can only take us so far. A good example is given in Ref. [6] where the authors adopt a perturbation scheme which is yet “too complex for general use". Numerical techniques are the only way out when dealing with realistic systems, e.g. systems where non-linear interactions prevail. To obtain information on what is proven to be an unfathomable quantity, a handful of recent studies have focused on numerical parametrization techniques aiming to decipher its main features. In principle, this can enable the numerical simulation of stochastic systems with a low computational cost compared to other methods [e.g. traditional agent-based simulations such as molecular dynamics (MD)].

Alas, the numerical front is not free of challenges. Despite its accuracy, the algorithm developed in Ref. [8] to parameterize GLEs involves sampling of the full high-dimensional system. Such an algorithm is $O(N)$-complex, which is not ideal for practical purposes as the computational costs grows (at least linearly) with the number of particles in the system. In Ref. [39], an iterative approach is adopted to compute a discrete/point-wise approximation of $\boldsymbol{\theta}(t)$ from the system's autocorrelation functions. However, this makes the convolution and the stochastic term of the GLEs computationally intractable, as they both depend on $\boldsymbol{\theta}(t)$. Finally, in Refs [25, 27] the authors propose to extract the memory kernel by Laplace transforming the correlation functions computed from historical data of the observables. While certainly interesting, this strategy exhibits serious limitations when the available data of the observables' dynamics are affected by even small fluctuations as we shall demonstrate.

Our overarching objective here is the development of a novel data-driven approach where the memory kernel is machine learned from observation data. For this purpose we propose the use of a feed-forward artificial neural network, namely a multilayer perceptron (MLP), to achieve an efficient and systematic forecasting of the memory kernel. We provide the MLP with appropriate historical data of the observables under study, obtained either from simulations or public databases. The MLP is then trained via an optimization process to approximate the memory kernel with a degree of accuracy depending on the number of neurons in the hidden layer. In particular, the memory kernel is extracted as an expansion of multi-exponential functions, which allows us to derive a tractable stochastic integration algorithm of a non-Markovian process characterized by time-correlated noise.

In this work, we present a novel data-driven approach, which makes use of the GLE structure coupled with a multilayer perceptron (MLP) to achieve an optimal parametrization of the memory kernel. The MLP is provided with proper historical data of the observables of interest obtained either from simulations or existing databases and then executes an optimization procedure to find the optimal approximation of the memory kernel. As we shown later in this section, compared to previous approaches our approximation through MLP shows enhanced robustness, especially when the available data are limited or affected by significant fluctuations. In the this procedure, the memory kernel is extracted in the form of a multi-exponential functions, thus enabling us to derive a tractable stochastic integration algorithm of the non-Markovian process characterized by a time-correlated noise. The universal approximation theorem [20, 19] guarantees a wide applicability of the our methodology which is tested in some relevant case studies from chemistry, biology, climatology and finance. These include: Modelling the dynamics of a single colloidal particle immersed in a heat bath of identical particles, also in presence of an external potential; Coarse-graining a particle chain in a bath; Modelling historical trends of a financial index.

Consider a system which has reached statistical equilibrium characterized by a stationary distribution $\rho(\mathbf{z})$. The historical data of the observables of the system, $\boldsymbol{\mathcal{O}}$, can be then be considered as a realization of a stationary process. With the aim of obtaining a direct relationship between $\boldsymbol{\theta}(t)$ and the statistics of the evolution of $\boldsymbol{\mathcal{O}}$, we can take the inner product of Eq. (17) and the observables' initial condition $\boldsymbol{\mathcal{O}}(0)$, yielding:

$$\begin{aligned}\mathbf{g}(t) &= -\langle \partial_t \boldsymbol{\mathcal{O}}(t) - \mathbf{F}(\boldsymbol{\mathcal{O}}(t)), \boldsymbol{\mathcal{O}}(0)\rangle \\ &= \left\langle \int_0^t \boldsymbol{\theta}(\tau)\boldsymbol{\mathcal{O}}(t-\tau)d\tau + \mathbf{R}(t), \boldsymbol{\mathcal{O}}(0)\right\rangle \\ &= \int_0^t \boldsymbol{\theta}(t-\tau)\mathbf{h}(\tau)d\tau, \end{aligned} \tag{19}$$

where $\mathbf{h}(t) = \langle \boldsymbol{\mathcal{O}}(t), \boldsymbol{\mathcal{O}}(0)\rangle$, $\mathbf{g}(t) - \langle \partial_t \boldsymbol{\mathcal{O}}(t) - \mathbf{F}(\boldsymbol{\mathcal{O}}(t)), \boldsymbol{\mathcal{O}}(0)\rangle$ is implicitly defined by the relation above, and $\langle \mathbf{R}(t), \boldsymbol{\mathcal{O}}(0)\rangle \sim \mathbf{0}$ because of the orthogonality between the random force and the initial value of the observables. For some specific cases (e.g. one-dimensional systems, or colloidal systems of spherical particles), $\boldsymbol{\theta}(t) = \theta(t)\mathbf{1}$, $\mathbf{g}(t) = g(t)\mathbf{1}$ and $\mathbf{h}(t) = h(t)\mathbf{1}$. For the sake of convenience we will then drop the identity operator $\mathbf{1}$ in such cases and simply use $\theta(t)$, $g(t)$ and $h(t)$.

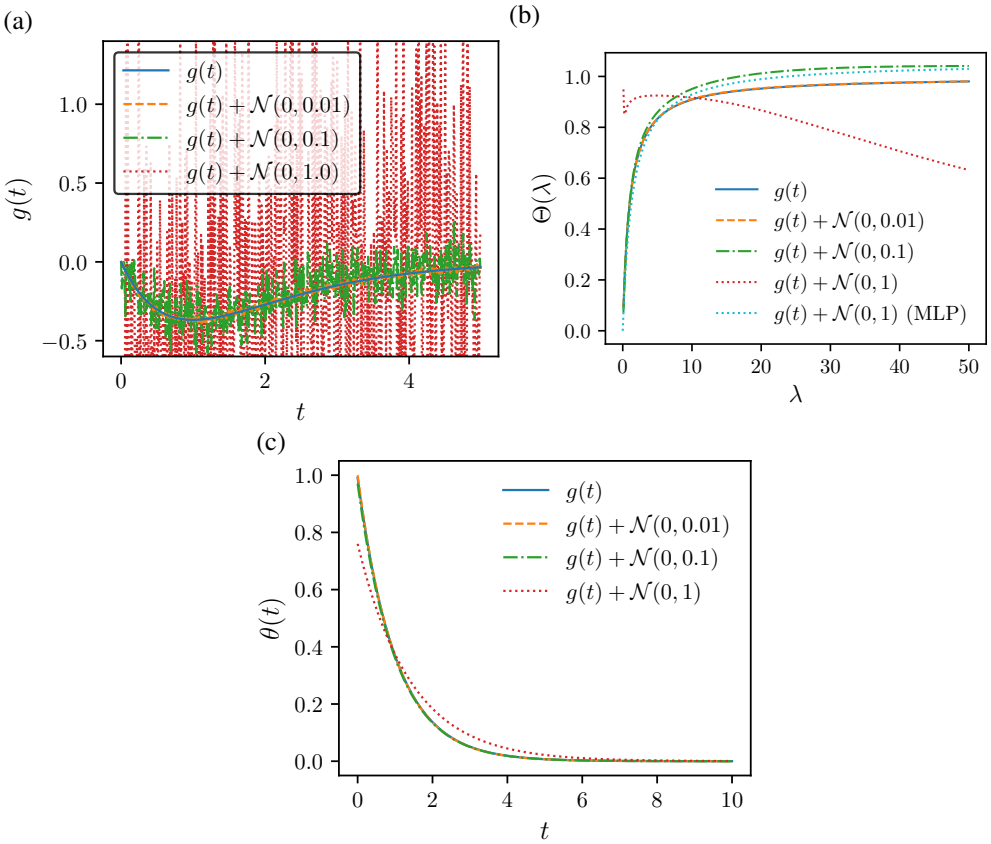

Figure 2: Convolution function $g(t)$ affected by random noise with varying amplitudes (a). Comparison between the memory kernel θ computed in the Laplace space (b) and with our MLP-based method (c), for $g(t)$ affected by a random noise with several amplitudes. For comparison purposes, we also report in (b) the Laplace transform of the memory kernel obtained with our MLP for strong noise, i.e. for noise variance $\sigma^2 = 1$.

1.3 Memory kernel in the Laplace space

Equation (19) can be rewritten by utilizing the properties of Laplace transform ($\mathcal{L}\{\boldsymbol{\mu}\}(\lambda) = \int_0^\infty \boldsymbol{\mu}(t)e^{-t/\lambda}$) which turns the convolution integral into a multiplication:

$$\mathbf{G}(\lambda) = \boldsymbol{\Theta}(\lambda)\,\mathbf{H}(\lambda) \Rightarrow \boldsymbol{\Theta}(\lambda) = \mathbf{G}(\lambda)\,\mathbf{H}(\lambda)^{-1} \tag{20}$$

where $\mathbf{G}(\lambda)$, $\boldsymbol{\Theta}(\lambda)$ and $\mathbf{H}(\lambda)$ are the Laplace transforms of $\mathbf{g}(t)$, $\boldsymbol{\theta}(t)$ and $\mathbf{h}(t)$, respectively. One approach is to adopt a rational function approximation for $\boldsymbol{\Theta}(\lambda)$ to be fitted to data, as was done by Lei *et al.*[27] This approximation seems to behave well in the absence of noise in the data. However, unfortunately this approach fails for limited data, which produce correlations affected by random noise. It is straightforward to demonstrate this serious limitation. Consider a function $\mathbf{g}(t)$ affected by a Gaussian source of uncertainty, $\boldsymbol{\epsilon}(t)$. This leads to an error in the Laplace transform, which can be expressed as $\Delta\boldsymbol{\Theta}(\lambda) = \tilde{\boldsymbol{\Theta}}(\lambda) - \boldsymbol{\Theta}(\lambda) = \boldsymbol{\mathcal{E}}(\lambda)\,\mathbf{H}^{-1}(\lambda)$, where $\boldsymbol{\mathcal{E}} = \mathcal{L}\{\boldsymbol{\epsilon}(t)\}$. For the sake of argument, assume that the Gaussian uncertainty can be expressed as the sum of non-systematic local errors, i.e. $\boldsymbol{\epsilon}(t) = \sum_i \boldsymbol{\epsilon}_i \delta(t - t_i)$, with $\boldsymbol{\epsilon}_i \sim \mathcal{N}(0, \sigma^2)$. Therefore, $\Delta\boldsymbol{\Theta}(\lambda) = \sum_i \boldsymbol{\epsilon}_i e^{-t_i/\lambda}\mathbf{H}^{-1}(\lambda)$. This clearly shows that local temporal errors turn into non-local contributions in the Laplace space. Such an *error propagation* will inevitably lead to significant inaccuracies that will compromise the rational approximation of the memory kernel. For instance, take the simple case $h(t) = e^{-t}$ which straightforwardly enables the analytical treatment of Eq. (19), $g(t) = -te^{-t}$ (see Fig. 2(a)). Figure 2(b) shows that the Laplace transform of the memory kernel (as computed in Ref. [27]) diverges from the actual curve as the noise intensity increases. Indeed the Laplace transform should be avoided. We shall demonstrate that the adoption of an MLP-based procedure provides an efficient and robust approximation of $\boldsymbol{\theta}$ in the time domain. Indeed, as illustrated in Fig. 2(c), the expected memory kernel is approximated very well even in the presence of strong noise in the underlying data.

1.4 Memory kernel extraction through MLP

Amongst the different possible neural network structures, MLPs have gained popularity because of their versatility and capability in approximating highly-nonlinear functions[33]. An MLP consists of at least three layers (known as input, hidden and output layers), each of them including several nodes or neurons (Fig. 1). The transformation of the dataset at each node is determined by an activation function, ϕ. Every node's inputs are weighted and added together with a bias, effectively an offset, to be finally passed through the activation function to compute its output. Training the network consists of finding the optimal weights and the biases which lead to minimize an appropriate cost (or error) function, computed at the output of the MLP. A popular choice for the cost function is the mean-square error (according to either Euclidean or non-Euclidean metrics). The iterations of the optimization process are known as epochs, and the whole procedure to find the optimal MLP parameterization is referred to as the *learning process*. We propose a three-layer MLP as a typical architecture for the multidimensional nonlinear regression problem of estimating the memory kernel. It should be highlighted that standard approaches model directly system data series (e.g. Ref. [18]), while our approach is different in that it integrates our physical knowledge of the phenomena at hand to extend the range of applicability of the model. As an example, consider a system in a known bistable potential for which we have access to data on system configurations in a single well only. With a standard approach, a machine learning model trained with these data would fail to detect bistability or estimate the transition time distribution. On the contrary, in our approach, a GLE embedded with a bi-stable potential and the extracted memory-kernel would be able to accurately model bi-stability and transition dynamics of such system.

The input of the MLP is a vector containing discrete time values, while the desired output is the function $g(t)$, which is known *a priori*. The hidden layer has an arbitrary number of neurons, determining the degree of accuracy of the memory-kernel approximation. As activation functions we use $\phi(z) = \int_0^t h(t-\tau)e^{z(\tau)}d\tau$ in the hidden layer, with $h(t)$ being known a priori and $\phi(z) = z$ at the output layer. The learning algorithm adopted is the resilient back-propagation algorithm with an adaptive learning rate.[34] Providing the MLP with the two matrices $\mathbf{g}(t)$ and $\mathbf{h}(t)$, an optimal approximator is obtained upon completion of the learning process. Such an estimator can be expressed as an exponential series, namely as $\boldsymbol{\theta}(t) \sim \sum_{k=1}^{N_n} \mathbf{A}_k e^{\mathbf{B}_k t}$, where N_n is the number of nodes in the hidden layer, $\mathbf{A}_k$ are matrices of real numbers and $\mathbf{B}_k$ are matrices with real negative coefficients (more details are given in the Supplementary Information). We now comment on the choice of the particular MLP configuration. This is because a three-layer MLP is the minimal network architecture satisfying the conditions of the universal approximation theorem. According to such a theorem, this network structure is able to approximate any continuous function defined on a compact subset of $\mathbb{R}^d$.[20, 19] Unfortunately, there are no formal results on the number of nodes required in the hidden layer to ensure the proper learning of the memory kernel function. But systematic experimentation gives the number that best worked in our case studies. It might seem counterintuitive, given the complexity of the prototypical examples we will consider, or even misleading, that the number of nodes needed in our experiments is just a few neurons. The main reason for this is that the major computational challenge would have been the learning of the dynamical law. However, this step is already made by the use of statistical mechanics which establishes the GLE as a general equation for the evolution of observable quantities and the description on non-Markovian Gaussian processes, making it possible to focus the computational effort on the learning of only a particular ingredient of the whole problem, namely the memory kernel. The simplest memory kernel one could employ is a Dirac delta function, which leads to the standard Langevin equation, i.e. the Markovian approximation of GLE. A realistic way of modelling memory kernels is by an exponentially decaying function, which weights each historical configuration based on its distance in time from the current state of the system. Approximating the memory kernel as a constant function is not realistic for physical systems as memory kernels represent the temporarily effects of a previous state of the system on the (implicit) environment. It is then not surprising that our MLP suggests approximating the memory kernel by the sum of few exponentially decaying functions. This works with a high degree of accuracy for complex systems.

1.5 Multi-layer perceptron structure and learning algorithm

Artificial neural networks are used for the parameterization of the GLE because of their enhanced capabilities to model non-linear relationships between system variables. Developed by analogy with biological processes in the brain, artificial neural networks are series of linear and non-linear transformations of some inputs to some outputs. Amongst the different possible variants, multi-layer perceptrons (MLPs) have gained popularity because of their potential and versatility in non-linear function approximations[33, 18]. MLPs consist of at least three layers, known as input, hidden and output layers, each one including more nodes. Each node i in the layer $l-1$ is connected with any other node j in the successive layer l and every connection is characterized by a parameter $w_{j,i}^l$ known as weight. In addition, for every neuron in the network there is a parameter known as the bias, b_j^l. The transformation of the dataset at each node is determined by an activation function, $\phi(z_j^l)$. It follows that the output a_j^l of the neuron j of the layer l is computed as

$a_j^l = \phi\left(z_j^l\right)$, with $z_j^l = \sum_i w_{j,i}^l a_i^{l-1} + b_j$. The network learning process then consists of an optimization algorithm aiming to find the weights $w_{j,i}^l$ and the biases b_j^l that minimize a cost (or error) function C computed at the output of the MLP. In this work, we employ a quadratic cost function $C = \sum_{t_j}^{N_t} \frac{1}{2N_t}\left(y_j(t_j) - a_j^L(t_j)\right)^2$, where N_t is the number of data samples. Hence, an algorithm is used to cyclically back-propagate the information about the error evaluated at the output to update weights and bias.

We adopt a three-layer MLP with a single input and a single output function. The hidden layer has an arbitrary number of neurons, N_n, determining the degree of accuracy of the memory kernel approximation. The universal approximation theorem guarantees that such a structure of the network is able to approximate any continuous function defined on a compact subset of $\mathbb{R}^d$[20, 19]. Initialization of the MLPs is achieved by providing Gaussian distributed random numbers to the weights and zeros of the biases. Moreover, no bias is added at the output layer. Regarding the activation function, in the hidden layer we adopt $\phi(z) = \int_0^t h(t-\tau)e^{z(\tau)}d\tau$, with $h(t)$ being known a priori, while at the output layer we employ $\phi(z) = z$.

For the learning process we adopt the resilient back-propagation algorithm Rprop[34] based on the gradient descent method, $\alpha_{e+1} = \alpha_e - \eta\nabla_\alpha C(\alpha_e)$, with the adaptive learning rate η,

$$\eta(e) = \begin{cases} \eta^+ \cdot \eta(e-1) & \text{if} \quad \frac{\partial C}{\partial \alpha}(e) \cdot \frac{\partial C}{\partial \alpha}(e-1) > 0, \\ \eta^- \cdot \eta(e-1) & \text{if} \quad \frac{\partial C}{\partial \alpha}(e) \cdot \frac{\partial C}{\partial \alpha}(e-1) < 0, \\ \eta(e-1) & \text{otherwise}, \end{cases} \tag{21}$$

where $\alpha = \left[w_{j,i}^l; b_j^l\right]$, and $0 < \eta^- < 1 < \eta^+$ are fixed parameters. From experience and following the literature[34], the Rprop algorithm gives an optimal compromise between calculation speed and solution convergence. Providing the MLP with the two matrices $\mathbf{g}(\mathbf{t})$ and $\mathbf{h}(\mathbf{t})$, the memory kernel is then extracted in the form of an exponential series:

$$\theta(t) \sim \sum_{k=1}^{N_n} w_k^3 e^{b_k^2} e^{w_k^2 t} = \sum_{k=1}^{N_n} A_k e^{B_k(t)}, \tag{22}$$

where N_n is the number of nodes in the hidden layer, $A_k = w_i^3 e^{b_k^2}$ are real coefficients and $B_k = w_k^2$ are real strictly negative quantities. The algorithm presented so far has been adopted to extract the memory kernel in the case of a diagonal $\boldsymbol{\theta}(t)$.

1.6 GLE time integration

The integration of the GLE dynamics is a non-trivial task for two reasons. First, the convolution integral depends on the full history of the observables. And second, the stochastic term is correlated in time. Different approaches have been proposed to address these issues for the scalar case [2, 22, 27]. In this work, we take advantage of the exponential structure of the identified $\boldsymbol{\theta}(t)$ to implement an integration algorithm. The history-dependent convolution term is then written as a sum of the additional variables $\mathbf{Z}_k(t)$, each defined as $\mathbf{Z}_k(t) = \int_0^t \mathbf{A}_k e^{\mathbf{B}_k(t-\tau)}\boldsymbol{\mathcal{O}}(\tau)d\tau$, so that their evolution equation can be expressed as $\dot{\mathbf{Z}}_k(t) = \mathbf{B}_k\mathbf{Z}_k(t) - \mathbf{A}_k\boldsymbol{\mathcal{O}}(t)$. The noise $\mathbf{R}(t)$ must satisfy the fluctuation-dissipation theorem. By introducing a set of auxiliary variables $\boldsymbol{\xi}_k(t)$, we can rewrite $\mathbf{R}(t) = \sum_{k=1}^{Nn}\mathbf{R}_k(t) = \sum_{k=1}^{Nn}\mathbf{b}_k\boldsymbol{\xi}(t)$, so that the corresponding evolution reads $\dot{\mathbf{R}}_k(t) = \mathbf{B}_k\mathbf{R}_k(t) + \mathbf{b}_k\boldsymbol{\xi}(t)$, where $\boldsymbol{\xi}(t)$ is a white noise with zero mean and time correlation $\langle\boldsymbol{\xi}(t)\boldsymbol{\xi}(s)\rangle = 2\langle\boldsymbol{\mathcal{O}},\boldsymbol{\mathcal{O}}\rangle\,\delta(t-s)$, while the coefficients $\mathbf{b}_k$ can be computed numerically (for details see Supplementary Information). By defining the variables $\mathbf{S}_k(t) = -\mathbf{Z}_k(t) + \mathbf{R}_k(t)$, the GLE can then be rewritten in the extended form:

$$\begin{cases} \dot{\boldsymbol{\mathcal{O}}}(t) & = \mathbf{F}(\boldsymbol{\mathcal{O}}(t)) + \sum_{k=1}^{N_n}\mathbf{S}_k(t) \\ \dot{\mathbf{S}}_k(t) & = \mathbf{B}_k\mathbf{S}_k(t) - \mathbf{A}_k\boldsymbol{\mathcal{O}}(t) + \mathbf{b}_k\boldsymbol{\xi}(t), \end{cases} \tag{23}$$

with $\mathbf{F}(\boldsymbol{\mathcal{O}}(t))$ accounting for the mean force contributions.

2 Numerical applications

2.1 Single particle in a bath

The first test to exemplify our methodology is a well-studied problem: the dynamics of a single colloidal particle (with mass m_B) immersed in a heat bath of n_b identical particles (with mass m_b). This problem also serves classically as model prototype for the derivation of the LE. The observable to be modelled with the MLP-enriched GLE of Eq.(17) is

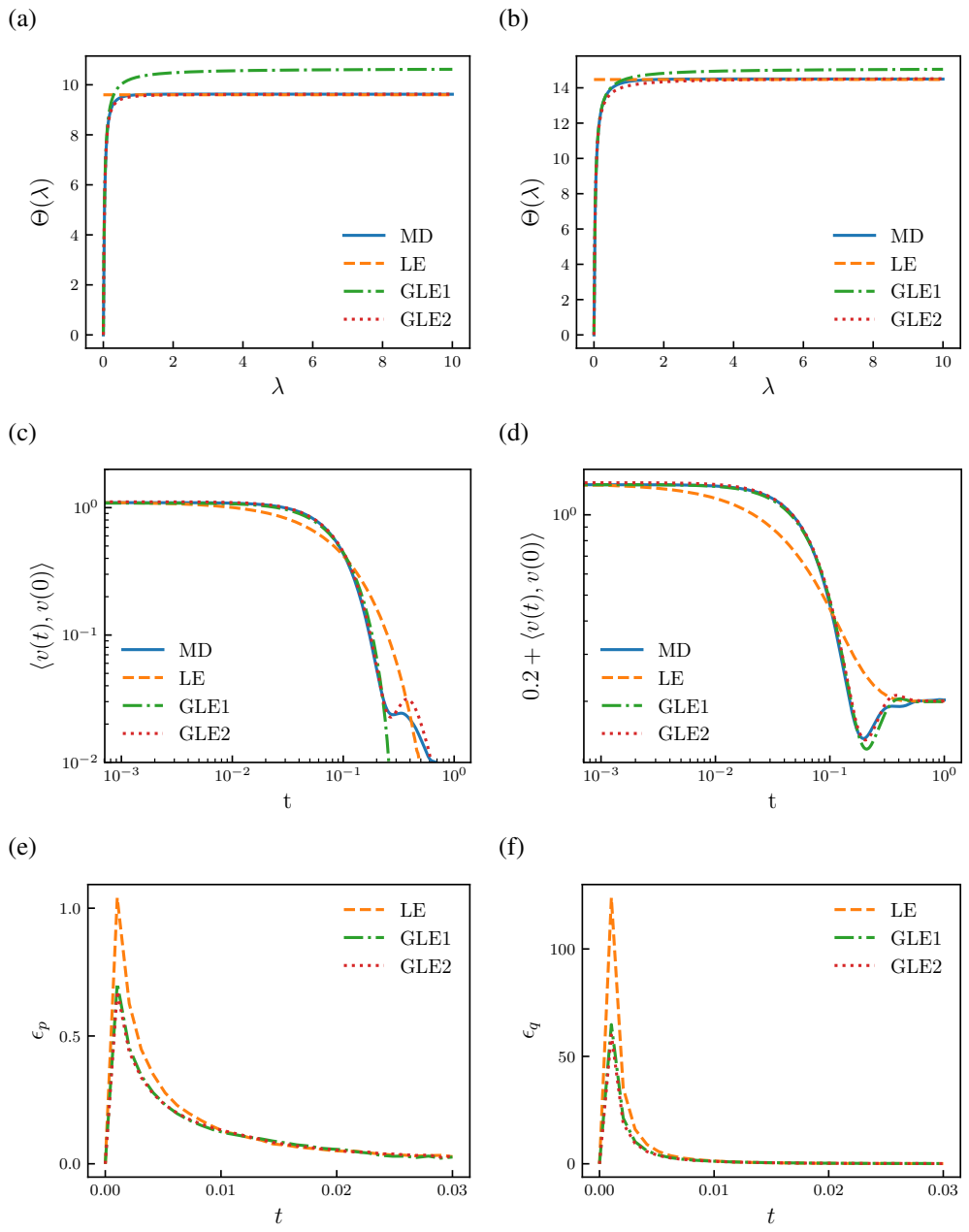

Figure 3: Memory kernels approximated through the MLP are compared against the ones obtained directly from MD simulation in the Laplace space, for (a) LDL and (b) HDL cases. Velocity correlation functions computed from MD, Langevin equation (LE) and GLE dynamics over 10^4 trajectories for both LDL (c) and HDL (d) cases are also reported. GLE1 and GLE2 refer to the memory kernel approximations obtained, respectively, with 1 and 2 neurons in the hidden layer. In (c) a constant factor of 0.2 is added to avoid negative values of the correlation in the log-log plot. In (e-f) we report the mean square differences $\epsilon_p(t)$ and $\epsilon_q(t)$ between the PDFs of the reduced systems (GLE and LE) and the exact pdf of the full system (MD) as function of the relaxation time.

the mean velocity of the colloidal particle, $v(t)$. while the historical data to be used for the training of the MLP are the values of the momenta of the target particle and forces acting on it generated with equilibrium molecular dynamics

Table 1: Value of the MLP error function after training for the LDL case.

Hidden nodes	Value of error function
1	6×10^{-2}
2	1×10^{-2}
3	1×10^{-2}
4	1×10^{-2}

(MD) simulations. The interaction between two particles i and j is modelled by the Lennard-Jones (LJ) potential:

$$v_{\mathrm{LJ}}(r) = \begin{cases} 4\epsilon \left[(\sigma/r)^{12} - (\sigma/r)^{6} \right] & \text{if } r \leq r_c, \\ 0 & \text{otherwise,} \end{cases} \tag{24}$$

where r is the distance between the particles, ϵ is the depth of the potential well, σ is the finite distance at which the inter-particle potential is zero and $r_c = 2.5\,\sigma$ is a cut-off radius. The numerical results are reported in reduced units, using σ and ϵ to scale lengths, energies and times, respectively. Our MD set-up is a cubic box of length $L = 10\,\sigma$ (hence volume $V = 10^3$), periodic boundary conditions along the Cartesian coordinates, x, y and z, and a Nosé-Hoover thermostat to equilibrate the system at a reduced temperature $T = 1.0$ (equivalent to $k_B T = \epsilon$). We consider two different scenarios depending on the bath particle densities: the low density limit (LDL) with $\rho_b = \frac{n_b}{V} = \frac{699}{1000}$, and the high density limit (HDL) with $\rho_b = \frac{799}{1000}$. The comparisons of the MLP-estimated and the exact/MD-extracted Laplace-transform of the memory kernels are shown in Figs 3(a)-(b) under LDL and HDL conditions, respectively. The use of the Laplace transform here is merely for comparison purposes, since we actually extract the memory kernel $\boldsymbol{\theta}(t)$ from our MD data. As can be readily checked in Figs 3(a)-(b), the first-order MLP approximator (GLE1) obtained with a single neuron at the hidden layer already outperforms the Markovian approximation (LE). Despite being already quite good, this first-order approximation is still unable to capture the behavior of $\boldsymbol{\Theta}(\lambda)$ for large values of λ. But just by adding a second neuron at the hidden layer, the second-order approximator (GLE2) perfectly converges to the exact MD results over the the whole λ-axis. In Table 1 we report the cost function error value after training. It can be noted that increasing the number of nodes in the hidden layer above 2 does not increase the accuracy of the MLPs approximation and additional nodes are redundant. As expected, the accuracy of the approximations (LE, GLE1 and GLE2) has a direct impact on the velocity correlation $\langle v(t), v(0) \rangle$ obtained, as shown in Figs 3(c)-(d). These figures clearly demonstrate the limitations of the Markovian approximation, which is quite different compared to the actual correlation decay. The first-order approximation is again fairly accurate, but diverges for long times. On the other hand, the second-degree approximation follows the exact autocorrelation within a tolerance lower than 1%. Having a very good estimation of the actual $\boldsymbol{\theta}(t)$, we can now proceed with the simulation of the reduced dynamics, i.e. the simulation of the MLP-enriched GLE, and compare with that obtained by MD simulations. For this purpose we simulate the GLE and MD dynamics out of equilibrium under the LDL. We analyze the time evolution towards equilibrium of the probability-density function (PDF) for the momentum and position, ϱ_p and ϱ_q, respectively, and as initial condition we chose a Dirac's delta distribution. In Figs 3(e)-(f), we show the standard errors for the momentum and position PDFs of the target particle, $\epsilon_\mu = ||\varrho_\mu^\nu - \varrho_\mu^{\mathrm{MD}}||$ with $\mu \in \{p, q\}$ and $\nu \in \{\text{LE, GLE1, GLE2}\}$. As can be clearly seen in the figures, our MLP-based GLE method dramatically reduces both errors ϵ_p and ϵ_q when compared to the Markovian approximation, up to a 50% lesser than LE during the non-equilibrium relaxation.

2.2 Particle in a bistable potential

As an additional validation of our GLE approach, we simulated a particle in a bath confined in a double well potential $U^{ext} = 10 \times (y^4 - y^2)$, and compared the GLE dynamics against MD, and against a neural-network forecasting of the dynamics by using NeuralProphet (a standard numerical library for data series modelling). NeuralProphet is based on an open-source software used for time data series forecasts by Facebook's core data science team[38]. It adopts an additive model where non-linear trends are fit with yearly, weekly, and daily seasonality, plus holiday effects. In Figure 4(a) we show a particle trajectory in the bistable potential simulated with MD (explicit bath particles), GLE embedded with a memory kernel approximated through our MLP (implicit bath particles) and NeuralProphet. This visualization shows that NeuralProphet cannot accurately reproduce the transition dynamics of the particle because of the non-seasonal behaviour of the original (MD) data series. In Figure 4(b), we also report the probability densities of the transition time, defined as the time difference between two consecutive crossings of the saddle point of the potential. This comparison between MD, GLE and NeuralProphet confirms that standard packages, such as NeuralProphet, cannot detect and replicate the full kinetics of transition dynamics dominated by non-seasonal events. On the contrary, our GLE approach shows its high capabilities in reproducing the MD transition time.

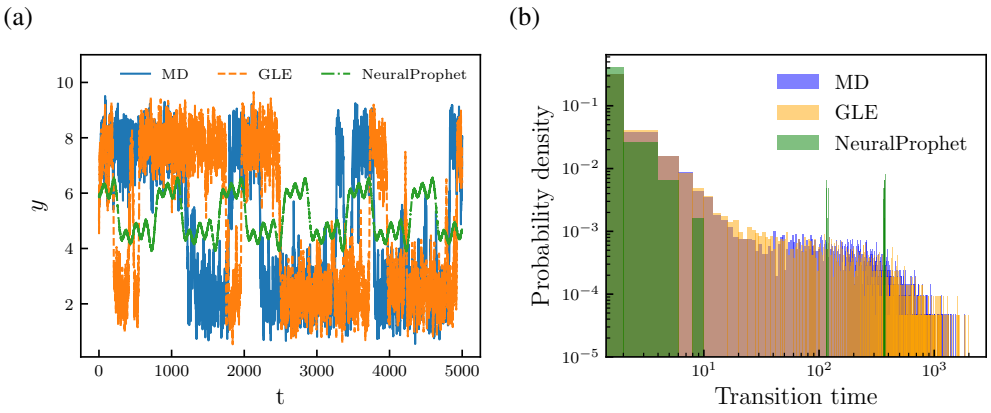

Figure 4: (a) Trajectory of a particle in a bistable potential simulated with MD (explicit bath particles), GLE embedded with a memory kernel approximated through our MLP (implicit bath particles) and a standard package using neural network for data series modelling (NeuralProphet). The comparison between transition time probability densities (b) shows that NeuralProphet cannot accurately reproduce the transition dynamics of the particle because of the non-seasonal behaviour of the original MD data series. On the contrary, the transition time distribution obtained with our GLE follows very closely the MD one.

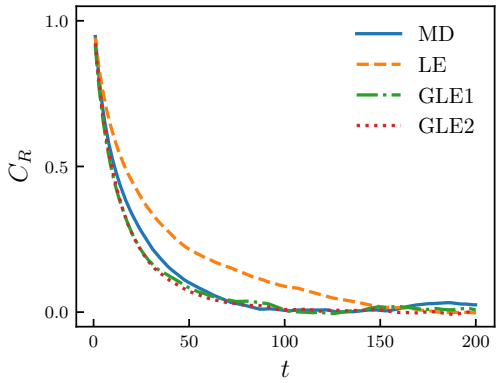

Figure 5: Time correlation of the gyration radius of a particle chain in a bath computed from LE, GLE and MD simulations.

2.3 Particle chain in a bath

Having established a very good performance for a single-particle dynamics, as the next step in testing our proposed MLP-enriched GLE formalism we look at the much more complex dynamics of a colloidal chain consisting of $N = 20$ particles immersed in a thermal bath. Particle chains are quite often used as prototypical systems to model polymers. In this context a widely used observable quantity for polymer characterization is the gyration radius, $R_G = \sqrt{\frac{1}{N}\sum_{k=1}^{N}(\mathbf{r}_k - \mathbf{r}_{\text{CM}})^2}$, where $\mathbf{r}_k$ and $\mathbf{r}_{\text{CM}}$ are the position vectors of the k-th particle and the center of mass of the chain, respectively. The increase in complexity of the "target particle" (a coarse-grained object, an aggregate of particles) brings about many complications when trying to derive an appropriate coarse-grained dynamical equation. We again rely upon the existence of a GLE which describes the time evolution of the observable, in this case R_G, and which needs to be trained with observed data, from MD in this particular case. For the MD simulations, we again make use of an LJ potential v_{LJ} to model pairwise non-bonded interactions amongst chain and bath particles. The chain particle interactions are given by the multi-body Dreiding potential[30] adopted in several studies (e.g. Ref. [21]) to study polymer-chains deformations including proteins in solution:

$$v(\mathbf{r}_{i,j,k,l}) = v_{\text{LJ}}(\mathbf{r}_{ij}) + v_H(\mathbf{r}_{ij}) + v_\theta(\mathbf{r}_{ijk}) + v_\phi(\mathbf{r}_{ijkl}), \tag{25}$$

where $v_H(\mathbf{r}_{ij}) = k_H(\mathbf{r}_{ij} - \mathbf{r}_0)^2$, $v_\theta(r_{ijk}) = k_\theta(\theta_{ijk} - \theta_0)^2$ and $v_\phi(r_{ijkl}) = k_\phi(1 + \cos(2\phi_{ijkl}))$ account for linear, angular and dihedral bonds, respectively (see Supplementary Information). The bath has the same characteristics ($\rho_b = \frac{699}{1000}$, and $T = 1.0$) as in the LDL introduced in the previous section. This choice, together with the assumption

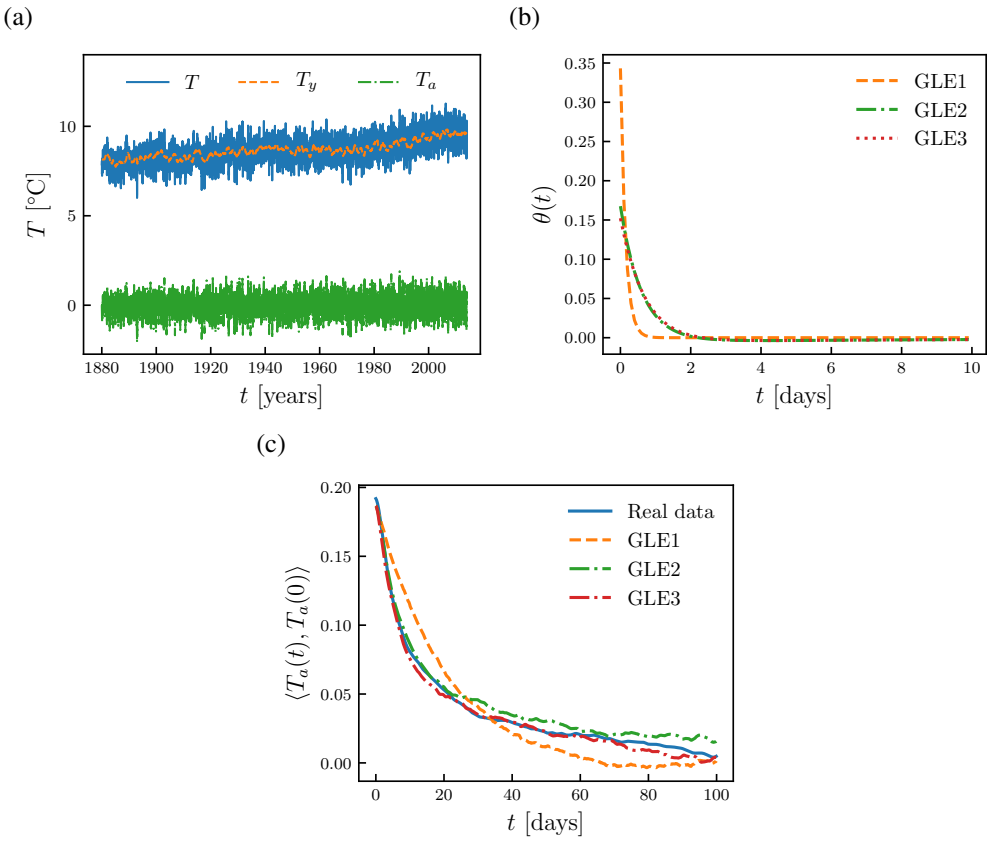

Figure 6: (a) Global temperature $T(t)$, annual moving average temperature $T_y(t)$ and the daily anomaly $T_a(t) = T(t) - T_y(t)$ between 1880 and 2014. (b) Memory kernel approximations computed through MLP with 1,2 and 3 neurons in the hidden layer and (c) corresponding time correlations obtained from real data and GLE simulations.

that the potential of mean force acting amongst the chain particles is approximately equal to $v(\mathbf{r}_{i,j,k,l})$, allows us to use the same memory kernel obtained for the single particle (see Fig. 3). With the MLP-approximated memory kernel fed into the GLE, we proceed with the simulation of the R_G dynamics, as we did for the single-particle case. The results of such simulations are used to compute and compare the gyration-radius autocorrelation[4, 9], $C_{R_G} = \left[\langle R_G^2(t)R_G^2(0)\rangle - \langle R_G^2(0)\rangle^2\right] / \left[\langle R_G^4(0)\rangle - \langle R_G^2(0)\rangle^2\right]$, extracted from the different (G)LE approximations (i.e., LE, GLE1 and GLE2) against the exact results obtained from MD. As can be readily checked in Fig. 5, in this case the GLE enriched with a one-neuron MLP already is able to accurately reproduce the bath effects on the chain, and clearly outperforms the commonly used Markovian approximation. The GLE2 model on the other hand seems to bring some regularization to the autocorrelation, making it smoother than the one obtained from GLE1, although both models seem to yield similar results. Evidently, even with the simplest MLP model we are able to capture the essence of the MD simulation, enabling us to carry out simulations with MD-like quality at almost no computational cost. The ease, but also convenience of our formalism, is indeed one of the most remarkable facts that should be highlighted.

2.4 Modelling global temperature

To illustrate now the versatility of our formalism we take a step away from our familiar particle dynamics examples in the search for phenomena and systems of general interest to look at. Our first stop is the forecasting of the earth-global temperature. Public attention aside, this is an interesting problem to tackle given that over the last few decades several stochastic Markovian models have been proposed to forecast global temperature dynamics, e.g. Refs [1, 31]. GLEs can be viewed as natural generalization of such models, although the memory kernel cannot be rigorously from first principles as in the case of prototypical statistical-physical problems. And the natural question of course here is what do GLEs have to do with climate. However, let us not forget the basic structure of GLEs: the dynamic variation of an observable quantity, a force, a drift, a term reflecting the history of the system and noise. The basic ingredients of most, if not all stochastic systems. But in the majority of the cases first-principles dynamical laws for stochastic systems –

the "*reductionist approach*" as was referred to by the authors in Ref. [24] – are just not possible. In such cases the "*complementary systems-based approach*" – again, referred to by the authors in Ref. [24] – is the only way out. But stipulating a model is not the end of the road, rather the beginning. The model needs to be properly parametrized and GLEs are not an exception. It is only then that they are capable of describing non-Markovian Gaussian processes and, thus, model general stochastic time series. Here we demonstrate that an MLP-enriched GLE is able to accurately describe the daily global-temperature fluctuations with respect to a properly chosen moving average (although our methodology can be also employed to model local temperature dynamics). Consider the daily land-average global temperature $T(t)$ measured during the period 1880-2014, published by Berkeley Earth[3, 35]. Despite the local temperature showing cyclical trends in short periods (e.g. due to to season changes), $T(t)$ does not exhibit a significant seasonal behavior, this being the result of the energy balance between solar and earth radiations[12]. Nevertheless, $T(t)$ reveals non-stationarity features due to a long-period increasing trend related to global warming, as observed in Fig. 6(a). We first compute the long term dynamics $T_y(t)$ as a yearly moving average. We then define the observable of interest as $T_a(t) = T(t) - T_y(t)$, so that the corresponding time series is stationary (see Supplementary Information). Hence, our proposal is to model the time evolution of $T_a(t)$ with the GLE $\partial_t T_a(t) = -\int_0^t \theta(t-\tau)T_a(\tau)d\tau + R(t)$. In fact, this is a generalization of the Markovian model for weather derivatives proposed in Ref. [1]. The different approximations of the memory kernel extracted from our MLP-based method are shown In Fig. 6(b), while Fig. 6(c) shows the corresponding correlation functions. We observe an excellent agreement between the correlations obtained with the GLE dynamics and the real-world data, especially when three neurons are adopted in the hidden layer (GLE3). Matching then the relaxation times of the memory kernel ($\sim$ days) with the characteristic time of the variable T_y ($\sim$ years), we can obtain the evolution of $T(t)$ as a sum of a Markovian yearly (long term) contribution and a non-Markovian daily (short term) contribution, namely:

$$\partial_t T(t) = (\partial_t + \theta_c)\, T_y(t) - \int_0^t \theta(t-\tau)T(\tau)d\tau + R(t), \tag{26}$$

where the constant is given by $\theta_c = \int_0^t \theta(\tau)$. Equation (26), originating directly from data, reflects the main features of global-temperature multi-scale dynamics and, thus, gives clear insights into current questions regarding, for instance, global warming. In fact, Eq. (26) can be used to distinguish between long-term temperature trends and short term fluctuations.

2.5 A stock market model: The Nikkei index

As expected, stochastic models have widely been employed to gain insight into financial instruments, such as bonds and stock prices[37, 26]. This is driven by the need that financial operations, such as financial risk management and portfolio optimization, require accurate predictions of markets dynamics to maximize profits. However, the majority of the models used in finance rely on Markovian assumptions, which can potentially introduce inaccuracies. Moreover, alternative standard approaches to model directly data series have a range of applicability limited by the training dataset. Here we use physics informed priors to integrate our experimental intuition of the phenomenon. Here we show that our methodology can overcome such limitations. As a case study here we adopt the GLE to model the daily price of the Japanese financial index Nikkei, $\mathrm{NI}(t)$, between May 1949 and May 2018[29]. As with many other financial instruments, $\mathrm{NI}(t)$ exhibits non-stationary behavior in both mean and variance. Assuming a local equilibrium approximation in the Nikkei trend (as we would do in Thermodynamics for a phenomenon at hand), we build an observable defined as $\mathrm{NI}_a(t) = [\mathrm{NI}(t) - \mathrm{NI}_y(t)]\,/\sigma_y(t)$, with $\mathrm{NI}_y(t)$ and $\sigma_y(t)$ being respectively a moving average and a moving standard deviation computed over a period $[t-y, t-1]$, respectively. The parameter y is then selected so as to obtain a stationary $\mathrm{NI}_a(t)$; we find $y = 10$ days to be the optimal value (details are given in the Supplementary Information. Hence, we model the normalized stock price $\mathrm{NI}_a(t)$ with the following non-Markovian model: $\partial_t \mathrm{NI}_a(t) = -\int_0^t \theta(t-\tau)\, \mathrm{NI}_a(\tau)d\tau + R(t)$. In Fig. 7(a), we report the observable $\mathrm{NI}_a(t)$ which exhibits a stationary Gaussian behavior (as verified in the Supplementary Information) and, thus, confirms our assumption of local equilibrium dynamics. Figures 7(b)-(c) show various degrees of approximations obtained with our framework and the corresponding correlation functions. In contrast with the global temperature trend, $\mathrm{NI}_a(t)$ do not exhibit a clear time-scale separation between the memory kernel and autocorrelation decay. The GLE dynamics shows a growing accuracy in representing the real data when the number of neurons in the hidden layer increases. As a matter of fact, already with the third-order approximation we are able to reproduce the correlation decay with a maximum relative error of order 10^{-2}. The proposed GLE equation, parameterized with an MLP equipped with 3 neurons, is then employed in a comparison between the predicted probability distribution and actual market data for four time windows, each ten market days long, between Jun 2018 and Aug 2018 (Fig. 7(d)). It is clear that our model is able not only to predict most of the actual market trend, but, crucially, to provide quite accurate information on the local variance of the trend, thus opening the way to optimizing risk management in short-term ($\sim$ weekly) investments.

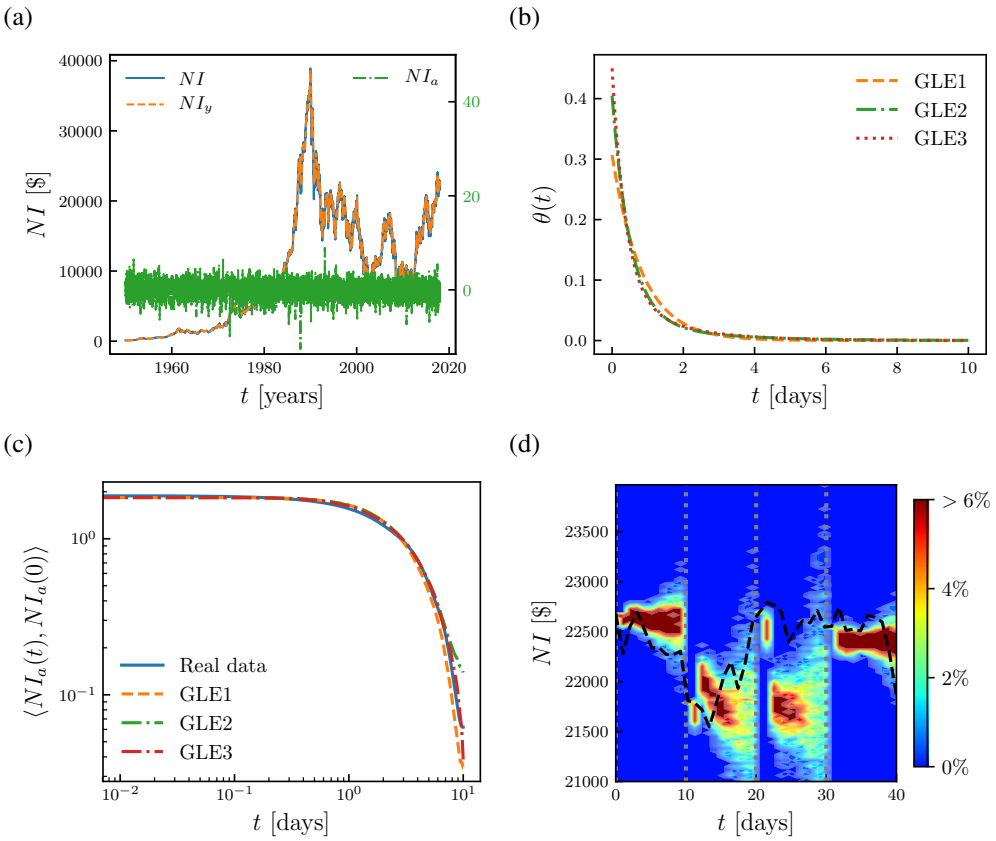

Figure 7: (a) Daily close price of Nikkei index $\mathrm{NI}(t)$, moving average index $\mathrm{NI}_y(t)$ computed over a window of ten days preceding the time t and the normalized index $\mathrm{NI}_a(t)$ between 1949 and 2018. (b) Memory kernel approximations computed through MLP with 1,2 and 3 neurons in the hidden layer and (c) the corresponding time correlations obtained from real data and GLE simulation. (d) Comparison between predicted probability distribution (color-map) and actual market data (dashed black line). Dotted lines in gray delineate the 10 days long investment windows.

3 Conclusions

We have introduced a novel methodology to decipher the analytically-intractable GLE dynamics. The basis of our framework is (a) stipulate GLEs as the fundamental underlying model for real-world stochastic systems, and (b) enriching GLEs with elements of machine learning such as neural networks. The universal approximation theorem guarantees the general applicability of our methodology. We have demonstrated that our machine-learning-enriched GLE is both accurate and efficient. But also robust when it comes to dealing with data affected by natural fluctuations which is typically the case with real-system data sets.

For convenience of the reader, the main steps required to apply the proposed methodology are listed below:

- Compute the matrices $\mathbf{g}(t)$ and $\mathbf{h}(t)$ (Sect.1.2) from a historical data series sampling the dynamical evolution of the observable of interest.
- Estimate the memory kernel function by means of a MLP with the structure described in Sect. 1.5
- Model the dynamical evolution of the system by employing a GLE embedded with the memory kernel computed in the previous step. For the integration in time of the GLE, one could follow the extended variables framework discussed in Sect.1.6

We have successfully tested our methodology against several prototypical examples: from standard problems like a single colloidal particle and particle chains in a bath, to climatology and finance. In all cases, we found excellent agreement between the actual and the approximated dynamics of the observables under consideration. Thus, coupling machine learning with a general equation of statistical mechanics, namely GLE, offers an attractive and versatile computational toolbox opening the door to a new way of modelling and understanding stochastic systems and, more

general, doing statistical mechanics. Future developments include relaxing the Markovian approximation in dynamic-density functional theory and fluctuating hydrodynamics[10, 14] but also adopting MLPs equipped with complex-valued exponential functions aiming to approximate oscillatory memory kernels.

Supplementary Information

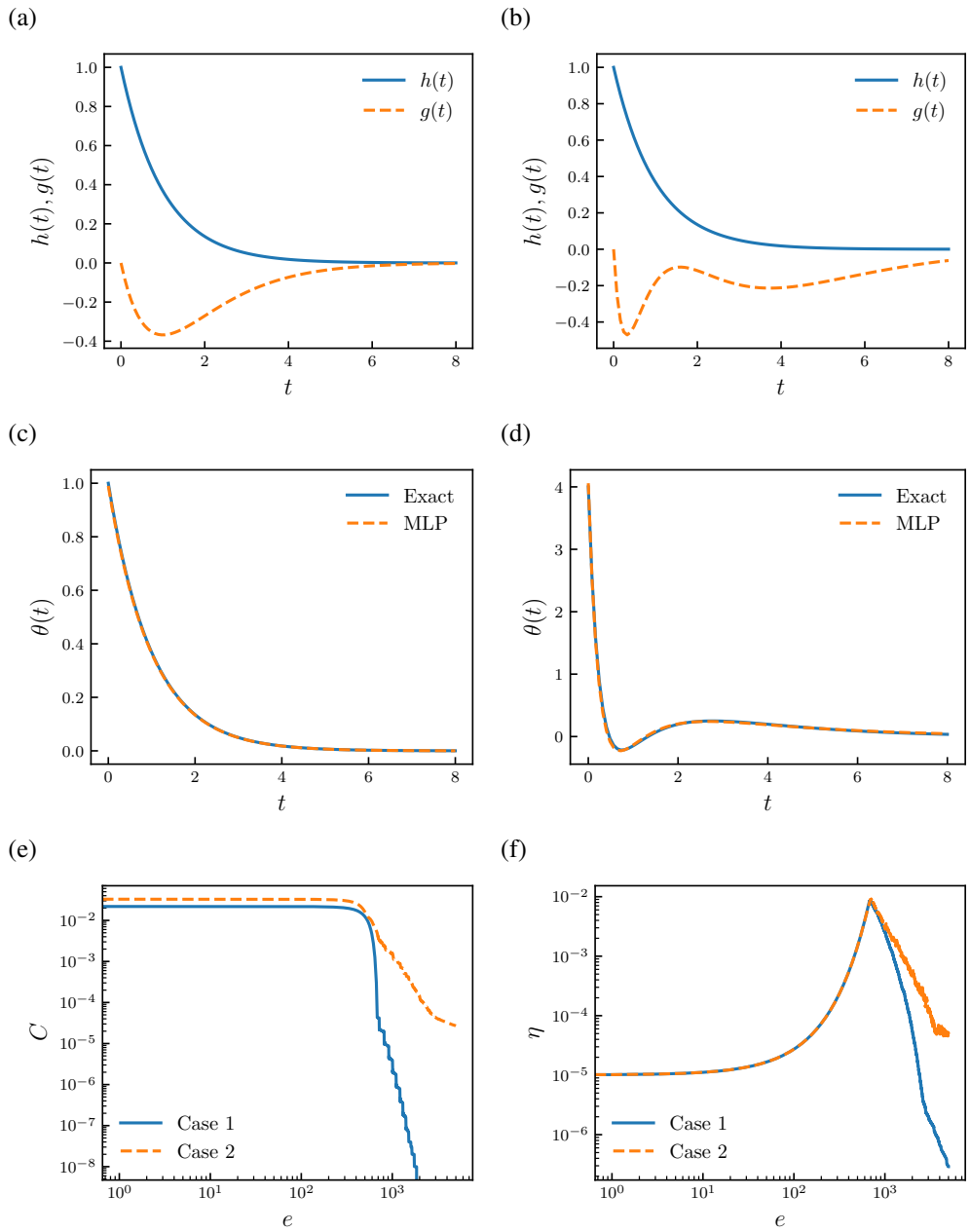

Figure 8: Two representative cases (discussed in the main text) to test our methodology: Case 1 in (a-c) and case 2 in (b-d). The functions $h(t)$ and $g(t)$ (a-b), discretized at 800 points, are provided to the MLP. The comparison between the memory kernel θ computed numerically with our MLP and the exact one is given in (c-d). In (e-f) we show the cost function and learning rate for the two analyzed scenarios. In both cases, the numerical approximation is obtained with an MLP trained for 5,000 epochs.

A Multi-layer perceptron structure: additional details and results

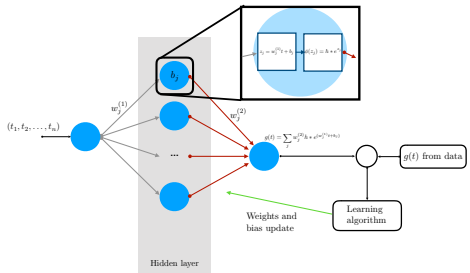

Figure 9: Representation of a MLP structure and the learning process

The structure of our MLPs is depicted in Fig. 9. The network training process is based on the updates of weights and biases. For the quadratic cost function the updates are defined as:

- error at the output layer: $\delta^{(3)} = \frac{\partial C}{\partial z^{(3)}} = \frac{\partial C}{\partial a^{(3)}} \frac{\partial a^{(3)}}{\partial z^{(3)}} = \frac{1}{N_t} \sum_{t_j}^{N_t} \left(y_j(t_j) - a_j^L(t_j) \right)$;
- error of the neuron j at the layer l: $\delta_j^l = \frac{\partial C}{\partial z_j^l} = \sum_k w_{j,i}^{l+1} \delta_k^{l+1} \frac{\partial \phi(z_j^l)}{\partial z_j^l}$;
- update of weight: $\Delta w_{j,i}^l = -\eta a_k^{l-1} \frac{\partial C}{\partial z_j^l}$;
- update of bias: $\Delta b_j^l = -\eta \frac{\partial C}{\partial z_j^l}$.

As a preliminary test of our approach, we consider three simple functions $h(t)$, $\theta(t)$ and $g(t)$ for which it can be shown analytically that $g(t) = -\int_0^t \theta(t-\tau) h(\tau) d\tau$. Given $h(t)$ and $g(t)$, an approximation of $\theta(t)$ is then computed with our methodology and is compared with the analytical $\theta(t)$. Two tests with different sets of functions are reported here. The functions used for the first test are:

$$h(t) = e^{-t}, \quad \theta(t) = e^{-t}, \quad g(t) = -te^{-t}. \tag{27}$$

In this test, because of the single exponential form of θ, an MLP with a single neuron in the hidden layer is used, namely $N_n = 1$.

The functions adopted for the second test are:

$$\begin{aligned} h(t) &= e^{-t}, \quad \theta(t) = 6e^{-4t} - 4e^{-t} + 2e^{-t/2}, \\ g(t) &= -\left(2e^{-t} - 2e^{-4t} - 4te^{-t} + 4e^{3t/2} - 4e^{-t} \right). \end{aligned} \tag{28}$$

For this latter example, we impose $N_n = 3$ neurons in the hidden layer.

Figures 8(a,b) report $h(t)$ and $g(t)$ provided as input to the MLP for both tests. The comparisons between numerical approximations and analytical θ reported in Fig. 8(c-d) clearly shows the accuracy of our methodology. The behaviors of cost function and learning rate during the learning process for both tests are also shown in Fig. 8(e-f).

B Numerical methods: GLE integration

Convolution decomposition As mentioned in the main text, the convolution term is written as a sum of the additional variable vectors $\mathbf{Z}_k(t)$, with $Z_{k,i}(t) = \int_0^t A_{k,ij} e^{B_{k,ij}(t-\tau)} \boldsymbol{\mathcal{O}}_j(\tau) d\tau$. Applying Leibniz's integral rule, and taking advantage of the symmetry of the matrices $\mathbf{B}_k$, it follows:

$$\dot{\mathbf{Z}}_k(t) = \mathbf{B}_k \mathbf{Z}_k(t) - \mathbf{A}_k \boldsymbol{\mathcal{O}}(t). \tag{29}$$

Hence, the original GLE is rewritten in the equivalent form:

$$\begin{cases} \partial_t \boldsymbol{\mathcal{O}}(t) = \mathcal{P}\mathcal{L}\boldsymbol{\mathcal{O}} - \sum_k \mathbf{Z}_k(t) + \mathbf{R}(t), \\ \partial_t \mathbf{Z}_k(t) = \mathbf{B}_k \mathbf{Z}_k(t) + \mathbf{A}_k \boldsymbol{\mathcal{O}}(t). \end{cases} \tag{30}$$

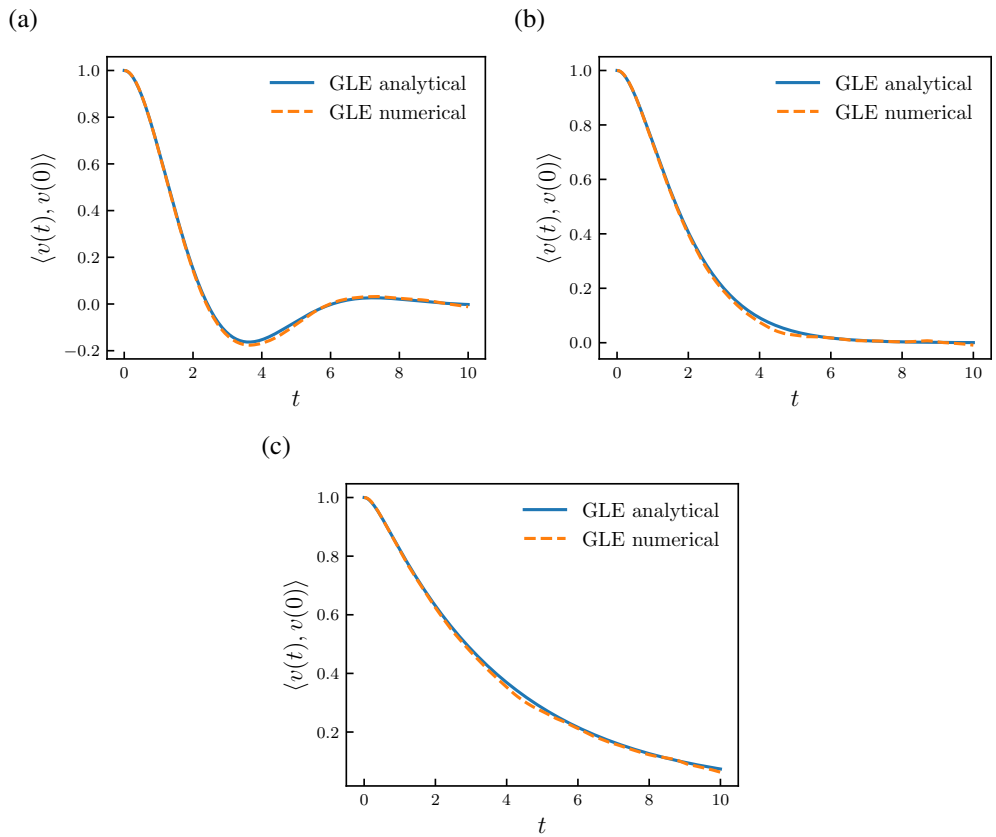

Figure 10: Comparison between numerical and analytical time correlation computed over 10^4 independent trajectories for a GLE with memory kernel in the form of a single exponential function [2]. The correlation is computed in the under-damped limit with A=1 and B=1 (a), in the damped case with A=1 and B=-2 (b), and in the over-damped limit with A=1 and B=-4 (c). In all cases the temperature is set to $T = 1$.

Random force decomposition We now turn to the theoretical derivation of the random force decomposition for a general real tensor function $\boldsymbol{\theta}(t)$. It is worth noticing that such formulation is valid for any form of the memory kernel, not just exponential ones. First, let us remark that, because of the symmetry between t and t' in the fluctuation-dissipation theorem, $\boldsymbol{\theta}(t)$ is an even function of time, i.e. $\boldsymbol{\theta}(t) = \boldsymbol{\theta}(-t)$. Let us now define the Fourier transform of $\boldsymbol{\theta}(t)$ as $\widetilde{\boldsymbol{\theta}}(\omega) = \int_{-\infty}^{-\infty} \boldsymbol{\theta}(t) e^{-i\omega\tau} dt$. Since $\boldsymbol{\theta}(t)$ is real and even in time, $\widetilde{\boldsymbol{\theta}}(\omega)$ is also real and even for real ω. It follows that both zeros and singular points of $\widetilde{\boldsymbol{\theta}}(\omega)$ are symmetric with respect to both real and imaginary axes in the ω-plane. We then introduce the function $\widetilde{\boldsymbol{\chi}}(\omega)$ given by

$$\widetilde{\boldsymbol{\chi}}(\omega) = \sum_k -i \left(\omega \mathbf{I} + i \mathbf{B'}_k\right)^{-1} \mathbf{b}_k, \tag{31}$$

where the real matrices $\mathbf{b}_k$ and $\mathbf{B'}_k$ are such that:

$$\widetilde{\boldsymbol{\theta}}(\omega) \langle \boldsymbol{\mathcal{O}}, \boldsymbol{\mathcal{O}} \rangle = 2 \widetilde{\boldsymbol{\chi}}(\omega) \widetilde{\boldsymbol{\chi}}^T(-\omega), \tag{32}$$

and the singular points of $\widetilde{\boldsymbol{\chi}}^{-1}(\omega)$ lie in the lower-half complex ω-plane. Moreover, we define the two matrices:

$$\widetilde{\boldsymbol{\zeta}}(\omega) = \widetilde{\boldsymbol{\chi}}^{-1}(\omega) = \sum_k \left(\omega \mathbf{I} + i \mathbf{B'}_k\right) \left(-i \mathbf{b}_k\right)^{-1}, \tag{33}$$

and

$$\widetilde{\mathbf{k}}_k(\omega) = -i \left(\omega \mathbf{I} + i \mathbf{B'}_k\right)^{-1} \mathbf{b}_k \widetilde{\boldsymbol{\zeta}}(\omega), \tag{34}$$

and we denote their Fourier inverse transform with $\boldsymbol{\zeta}(t)$ and $\mathbf{k}_k(t)$. Combining Eqs (31), (33) and (34), it follows that:

$$\sum_k \widetilde{\mathbf{k}}_k(\omega) = \mathbf{I} \tag{35}$$

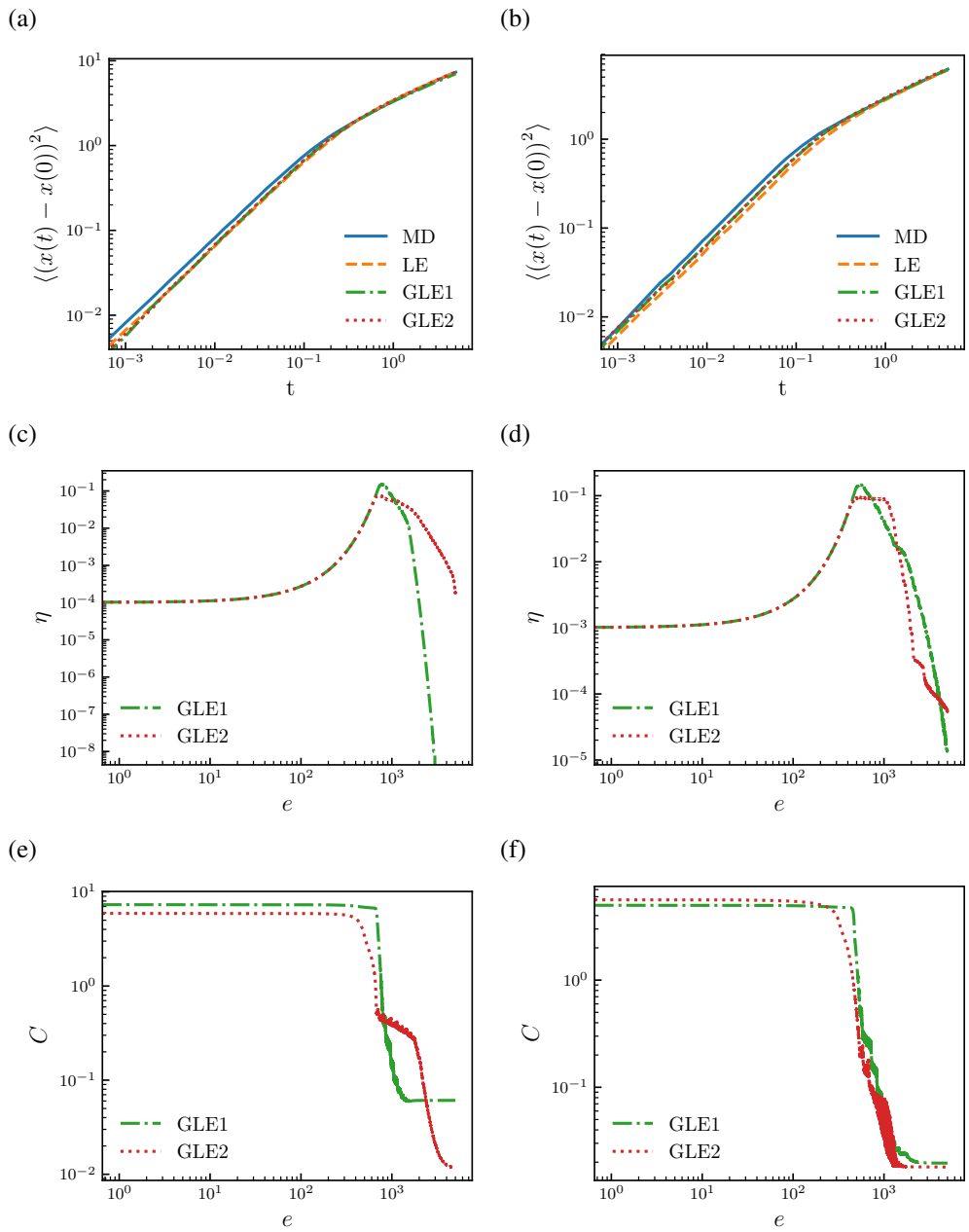

Figure 11: Comparison of the mean-square displacement MSD computed with the MLP and with MD, for both LDL (a) and HDL (b) cases. GLE1 and GLE2 refer to the memory kernel approximations obtained with 1 and 2 neurons in the hidden layer, respectively.

or, equivalently,

$$\sum_k \mathbf{k}_k(t) = \mathbf{I}\delta(t). \tag{36}$$

Moreover Eq. (34) can be rewritten as $(i\omega\mathbf{I} - \mathbf{B'}_k)\,\widetilde{\mathbf{k}}_k(\omega) = \mathbf{b}_k\widetilde{\boldsymbol{\zeta}}(\omega)$, that in the time domain gives:

$$\frac{d}{dt}\mathbf{k}_k(t) - \mathbf{B'}_k\mathbf{k}_k(t) = \mathbf{b}_k.\boldsymbol{\zeta}(t) \tag{37}$$

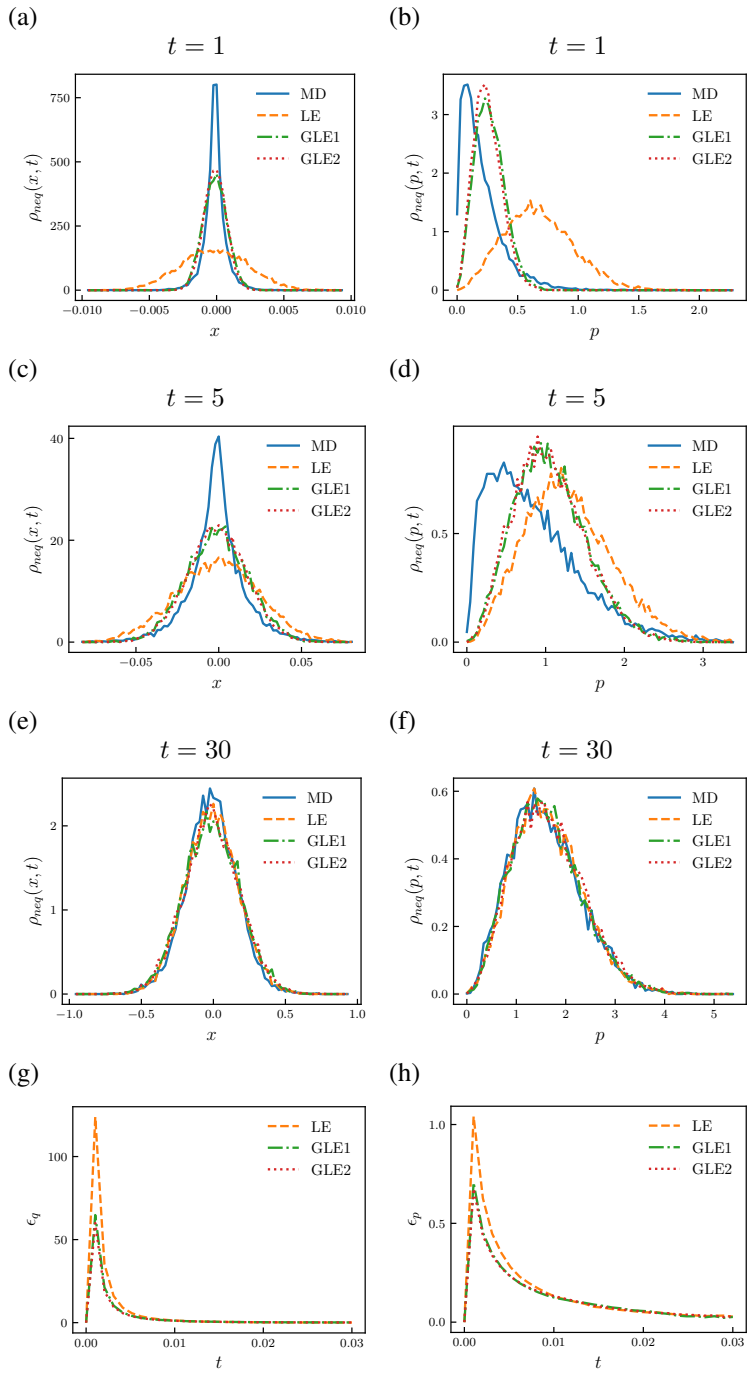

Figure 12: Relaxation dynamics of position (a-c-e) and momentum (b-d-f) PDF from Dirac delta to equilibrium computed with MD, LE and GLE over 10^4 trajectories. Corresponding mean square error of position (g) and momentum (h) PDF in time.

Finally, the following vector variables are introduced:

$$\boldsymbol{\xi}(t) = \int_0^{+\infty} \boldsymbol{\zeta}(t-t')\mathbf{R}(t')dt', \tag{38}$$

and

$$\mathbf{R}_k(t) = \int_0^{+\infty} \mathbf{k}_k(t-t')\mathbf{R}(t')dt'. \tag{39}$$

From Eq. (39) and Eq. (36) it follows that:

$$\sum_k \mathbf{R}_k(t) = \mathbf{R}(t), \tag{40}$$

while, combining Eq. (39) and Eq. (37)

$$\frac{d}{dt}\mathbf{R}_k(t) = \mathbf{B'}_k\mathbf{R}_k(t) + \mathbf{b}_k\boldsymbol{\xi}(t). \tag{41}$$

Equations $(40-41)$ are our main result here. They allow to express the correlated noise of the original GLE as a function of white noise $\boldsymbol{\xi}(t)$.

In what follows, we discuss the properties of the stochastic process $\boldsymbol{\xi}(t)$. First, since all the singularities of $\widetilde{\boldsymbol{\zeta}}(\omega) = \widetilde{\boldsymbol{\chi}}^{-1}(\omega)$ lie in the lower-half complex ω-plane, it follows that for $\tau > 0$ we have:

$$\begin{aligned}
\boldsymbol{\zeta}(\tau) &= \frac{1}{2\pi}\int_{-\infty}^{\infty} d\omega \widetilde{\boldsymbol{\zeta}}(\omega)e^{i\omega\tau} \\
&= \lim_{a\to\infty}\frac{1}{2\pi}\int_{-a}^{a} d\omega \widetilde{\boldsymbol{\zeta}}(\omega)e^{i\omega\tau} = \\
&= \frac{1}{2\pi}\oint_{C^+} d\omega \widetilde{\boldsymbol{\zeta}}(\omega)e^{i\omega\tau} \\
&- \lim_{a\to\infty}\frac{1}{2\pi}\int_{\text{arc}(a\to -a)} d\omega \widetilde{\boldsymbol{\zeta}}(\omega)e^{i\omega\tau} = \mathbf{0},
\end{aligned} \tag{42}$$

where $\oint_{C^+} d\omega$ indicates the integral over a closed contour C^+ along the real line from $-a$ to a and then along a circular arc at 0 from a to $-a$ and in the upper half-plane, $\int_{\text{arc}(a\to -a)} d\omega$. Hence, for $t > 0$ we can write

$$\begin{aligned}
\boldsymbol{\xi}(t) &= \int_0^{+\infty} \boldsymbol{\zeta}(t-t')\mathbf{R}(t')dt' \\
&= \int_{-\infty}^{+\infty} \boldsymbol{\zeta}(t-t')\mathbf{R}(t')dt'.
\end{aligned} \tag{43}$$

Thus, the correlation function of $\boldsymbol{\xi}(t)$ at t_1 and t_2 is given by:

$$\begin{aligned}
\left\langle \boldsymbol{\xi}(t_1)\boldsymbol{\xi}^T(t_2)\right\rangle &= \int_{-\infty}^{+\infty} dt_1' \int_{-\infty}^{+\infty} dt_2' \boldsymbol{\zeta}(t_1-t_1')\times \\
&\left\langle \mathbf{R}(t_1')\mathbf{R}^T(t_2')\right\rangle \boldsymbol{\zeta}^T(t_2-t_2') = \\
&= \int_{-\infty}^{+\infty} dt_1' \int_{-\infty}^{+\infty} dt_2' \boldsymbol{\zeta}(t_1-t_1')\boldsymbol{\theta}(t_1'-t_2')\times \\
&\langle \boldsymbol{\mathcal{O}}, \boldsymbol{\mathcal{O}}\rangle \boldsymbol{\zeta}^T(t_2-t_2'),
\end{aligned} \tag{44}$$

where we used the fluctuation-dissipation theorem. From the definition of Fourier transform of $\boldsymbol{\theta}$, it follows

$$\begin{aligned}\left\langle \boldsymbol{\xi}(t_1)\boldsymbol{\xi}^T(t_2)\right\rangle = &\int_{-\infty}^{+\infty} dt_1' \int_{-\infty}^{+\infty} dt_2' \boldsymbol{\zeta}(t_1-t_1')\times \\ &\frac{1}{2\pi}\int_{-\infty}^{+\infty} d\omega \widetilde{\boldsymbol{\theta}}(\omega) e^{i\omega(t_1'-t_2')}\langle \boldsymbol{\mathcal{O}},\boldsymbol{\mathcal{O}}\rangle \times \\ &\boldsymbol{\zeta}^T(t_2-t_2') = \\ &= \int_{-\infty}^{+\infty} dt_1' \int_{-\infty}^{+\infty} dt_2' \boldsymbol{\zeta}(t_1-t_1')\times \\ &\frac{1}{2\pi}\int_{-\infty}^{+\infty} d\omega \widetilde{\boldsymbol{\theta}}(\omega) e^{i\omega(t_1'-t_2')}\langle \boldsymbol{\mathcal{O}},\boldsymbol{\mathcal{O}}\rangle \boldsymbol{\zeta}^T(t_2-t_2')\times \\ &e^{-i\omega(t_1-t_2)}e^{i\omega(t_1-t_2)} = \\ &= \frac{1}{2\pi}\int_{-\infty}^{+\infty} d\omega \int_{-\infty}^{+\infty} dt_1' \boldsymbol{\zeta}(t_1-t_1')\times \\ &e^{-i\omega(t_1-t_1')}\widetilde{\boldsymbol{\theta}}(\omega)\langle \boldsymbol{\mathcal{O}},\boldsymbol{\mathcal{O}}\rangle \int_{-\infty}^{+\infty} dt_2' \boldsymbol{\zeta}^T(t_2-t_2')\times \\ &e^{i\omega(t_2'-t_2')}e^{i\omega(t_1-t_2)}.\end{aligned} \tag{45}$$

Applying the definition of Fourier transform of $\boldsymbol{\zeta}(t)$, and taking advantage of Eq. (32) and Eq. (33), we finally obtain:

$$\begin{aligned}\left\langle \boldsymbol{\xi}(t_1)\boldsymbol{\xi}(t_2)^T\right\rangle = &\frac{1}{2\pi}\int_{-\infty}^{+\infty} d\omega \widetilde{\boldsymbol{\zeta}}(\omega)\widetilde{\boldsymbol{\theta}}(\omega)\langle \boldsymbol{\mathcal{O}},\boldsymbol{\mathcal{O}}\rangle \\ &\widetilde{\boldsymbol{\zeta}}^T(-\omega)e^{i\omega(t_1-t_2)} = \\ = &\frac{1}{2\pi}\int_{-\infty}^{+\infty} d\omega \widetilde{\boldsymbol{\zeta}}(\omega) 2\widetilde{\boldsymbol{\chi}}(\omega)\widetilde{\boldsymbol{\chi}}(-\omega)^T \\ &\widetilde{\boldsymbol{\zeta}}^T(-\omega)e^{i\omega(t_1-t_2)} \\ = &\frac{1}{2\pi}\int_{-\infty}^{+\infty} d\omega 2\mathbf{I} e^{i\omega(t_1-t_2)} = 2\delta(t_1-t_2).\end{aligned} \tag{46}$$

It follows that $\boldsymbol{\xi}(t)$ is a delta-correlated stochastic process, thus generalizing the work by Kawai [22] to a tensorial memory kernel.

As we adopted an approximation of $\boldsymbol{\theta}(t)$ whose components are in the exponential form $\theta_{i,j}(t) = \sum_k A_{k,ij} e^{B_{k,ij}(t)}$, its Fourier transform is given by:

$$\widetilde{\boldsymbol{\theta}}(\omega) = \sum_k \left[-i\mathbf{A}_k \oslash (\omega\mathbf{J} + i\mathbf{B}_k) + i\mathbf{A}_k \oslash (\omega\mathbf{J} - i\mathbf{B}_k)\right], \tag{47}$$

where $\oslash$ indicates the Hadamard division and $\mathbf{J}$ is an all-ones $n \times n$ matrix. Since $\boldsymbol{\theta}(t)$ is a real and even function of t, $\widetilde{\boldsymbol{\theta}}(\omega)$ has to be real and even for real values of ω. As a consequence, the singular points of $\widetilde{\boldsymbol{\theta}}(\omega)$ have to be symmetric with respect to the real and imaginary axes, namely in the form of pairs, $\pm i\mathbf{B}_k$. For the same reason, the roots of $\widetilde{\boldsymbol{\theta}}(\omega)$ have to be symmetric with respect to the real and imaginary axes. Thus, putting Eq. (47) into a common denominator, factorizing, and using $\boldsymbol{\beta}_n$ and $\boldsymbol{\beta}_n^*$ to denote the conjugate matrices containing the zeros of the numerator, yields:

$$\begin{aligned}\widetilde{\boldsymbol{\theta}}(\omega) = &\mathbf{K} \odot \left(\prod_n (\omega\mathbf{J} - \boldsymbol{\beta}_n) \odot (\omega\mathbf{J} - \boldsymbol{\beta}_n^*)\right) \\ &\oslash \left(\prod_k (\omega\mathbf{J} + i\mathbf{B}_k) \odot (\omega\mathbf{J} - i\mathbf{B}_k)\right),\end{aligned} \tag{48}$$

where $\odot$ is the Hadamard product, $\mathbf{K}$ is a matrix of positive real numbers and it is assumed that $\mathrm{Im}(\beta_n) > 0$ and $\mathrm{Im}(\beta_n^*) < 0$. It is worth noticing that since $\widetilde{\boldsymbol{\theta}}(\omega)$ is non-negative $\mathbf{K}$ contains positive values only [22]. Define now the

function $\widetilde{\boldsymbol{\chi}}(\omega)$ as:

$$\begin{aligned}\widetilde{\boldsymbol{\chi}}(\omega) =& \frac{\mathbf{K}^{1/2}}{\sqrt{2}} \odot \langle \boldsymbol{\mathcal{O}}, \boldsymbol{\mathcal{O}} \rangle^{\odot 1/2} \odot \prod_n i\left(\omega \mathbf{J} - \boldsymbol{\beta}_n^*\right) \\ & \oslash \prod_k i\left(\omega \mathbf{J} + i\mathbf{B}_k\right) = \\ & \sum_k -i\left(\omega \mathbf{I} + i\mathbf{B}_k\right)^{-1} \mathbf{b}_k.\end{aligned} \tag{49}$$

Equation (49) has to be solved to find the matrices $\mathbf{b}_k$.

In the case of diagonal memory kernel matrix, $\mathbf{b}_k$ can be straightforwardly obtained by solving:

$$\begin{aligned}\frac{\mathbf{K}^{1/2}}{\sqrt{2}} \langle \boldsymbol{\mathcal{O}}, \boldsymbol{\mathcal{O}} \rangle^{1/2} \prod_n i\left(\omega \mathbf{I} - \boldsymbol{\beta}_n^*\right) \prod_k i\left(\omega \mathbf{I} + i\mathbf{B}_k\right)^{-1} = \\ \sum_k -i\left(\omega \mathbf{I} + i\mathbf{B}_k\right)^{-1} \mathbf{b}_k.\end{aligned} \tag{50}$$

Finally, for a one-dimensional GLE the presented formulation reduces to the one derived by Kawai [22], therefore the coefficients b_k can be evaluated from the following relation:

$$\langle \boldsymbol{\mathcal{O}}, \boldsymbol{\mathcal{O}} \rangle A_k = -2b_k \sum_n \frac{b_n}{B_k + B_n}, \tag{51}$$

obtained by Eqs (31), (32) and (47).

Extended dynamics and integration algorithm For a general $\boldsymbol{\theta}(t)$, we have the following extended dynamics:

$$\begin{cases} \partial_t \boldsymbol{\mathcal{O}}(t) = \mathcal{P}\mathcal{L}\boldsymbol{\mathcal{O}} - \int_0^t \boldsymbol{\theta}(\tau)\boldsymbol{\mathcal{O}}(t-\tau)d\tau + \sum_k \mathbf{R}_k(t), \\ \partial_t \mathbf{R}_k(t) = \mathbf{B'}_k \mathbf{R}_k(t) + \mathbf{b}_k \boldsymbol{\xi}(t), \end{cases} \tag{52}$$

where the convolution can be decomposed in different ways depending on the structure of $\boldsymbol{\theta}(t)$. In our case $\boldsymbol{\theta}(t)$ has an exponential form, thus $\mathbf{B'}_k = \mathbf{B}_k$ and the variables $\mathbf{S}_k(t) = -\mathbf{Z}_k(t) + \mathbf{R}_k(t)$ can be defined so that the GLE is rewritten in the following form:

$$\begin{cases} \partial_t \boldsymbol{\mathcal{O}}(t) = \mathbf{F}(\boldsymbol{\mathcal{O}}(t)) + \sum_{k=1}^{N_n} \mathbf{S}_k(t), \\ \partial_t \mathbf{S}_k(t) = \mathbf{B}_k \mathbf{S}_k(t) - \mathbf{A}_k \boldsymbol{\mathcal{O}}(t) + \mathbf{b}_k \boldsymbol{\xi}(t), \end{cases} \tag{53}$$

with $\mathbf{F}(\boldsymbol{\mathcal{O}}(t)) = \mathcal{P}\mathcal{L}\boldsymbol{\mathcal{O}}$ accounting for the conservative mean force contributions.

The numerical algorithm adopted to solve the system in Eq. (53) involves a splitting scheme together with the Euler-Maruyama scheme for the stochastic part, $S_k(t)$:

$$\boldsymbol{\mathcal{O}}^{(n+1/2)} = \boldsymbol{\mathcal{O}}^{(n)} + \frac{\Delta t}{2} F^c(\boldsymbol{\mathcal{O}}^{(n)}) + \frac{\Delta t}{2} \sum_{k=1}^{N_n} S_k^{(n)}, \tag{54}$$

$$S_k^{(n+1)} = \left(1 + B_k \Delta t\right) S_k^{(n)} - A_k \boldsymbol{\mathcal{O}}^{(n+1/2)} \Delta t + b_k \xi_k^{(n)}, \tag{55}$$

$$\boldsymbol{\mathcal{O}}^{(n+1)} = \boldsymbol{\mathcal{O}}^{(n+1/2)} + \frac{\Delta t}{2} F^c(\boldsymbol{\mathcal{O}}^{(n+1)}) + \frac{\Delta t}{2} \sum_{k=1}^{N_n} S_k^{(n+1)}, \tag{56}$$

where $\xi_k^{(n)} \sim \mathcal{N}(0, 2\Delta t)$ are independent Gaussian distributed random values.

To test the numerical stochastic integrator, similarly to Ref. [2], we consider a one-dimensional GLE with a single exponential memory kernel and no conservative forces. In this specific case, the time correlation is analytically solvable:

$$\frac{\langle \boldsymbol{\mathcal{O}}(t)\boldsymbol{\mathcal{O}}(0) \rangle}{\langle \boldsymbol{\mathcal{O}}(0)\boldsymbol{\mathcal{O}}(0) \rangle} = \begin{cases} e^{\frac{tB}{2}} \left(\cos(\Omega t) - \frac{B}{2\Omega} \sin(\Omega t)\right) & \Omega \neq 0, \\ e^{\frac{tB}{2}} \left(1 - \frac{Bt}{2}\right) & \Omega = 0, \end{cases} \tag{57}$$

where the complex parameter $\Omega = \sqrt{A - B^2/4}$ was introduced. Figure 10 shows that the numerical integrator is able to accurately reproduce the analytical correlation in the under-damped limit ($A = 1$ and $B = 1$), in the damped case ($A = 1$ and $B = -2$) and in the over-damped limit ($A = 1$ and $B = -4$).

Table 2: Values of the interaction potentials parameters, adopted to simulate the particle chain.

Parameters	K_H	K_γ	K_ϕ	r_0	γ_0	$\epsilon_{i,j}$	$\sigma_{i,j}$
Values	100	10	10	1.5	109.5	1	1

C Single particle in a bath: simulation details and additional results

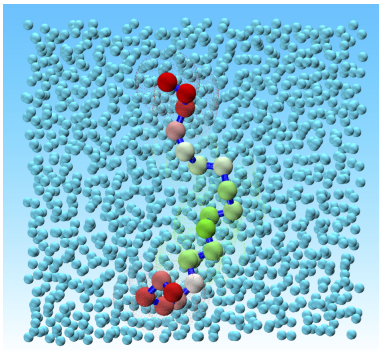

Figure 13: Representation of a particle chain at equilibrium with a heat bath.

A target colloidal particle, with mass $m = 1$, is immersed in a bath of identical particles with masses $m_b = 1$. Two systems are studied. We simulate a low density limit (LDL) with 700 particles in total, while the high density limit (HDL) with 800 particles. The interaction between any two particles i and j is modelled by the Lennard-Jones (LJ)potential. MD simulations were performed integrating particles governing equations in time by using a Verlet algorithm. The time step is fixed at $\Delta t = 10^{-3}$. The following procedure is then adopted for the MD simulations. First, the bath particles are randomly generated inside the simulation box. Then, a minimization algorithm is employed to avoid overlaps between particles. Hence, a run of 10^5 time steps is used to equilibrate the system. Finally, data on forces and momenta are gathered over 10^5 time steps. This process is repeated for 10^2 trajectories in order to enhance the accuracy of the correlations, and consequently, of the memory kernels.

In Figs 11(a,b) we report the mean-square displacement (MSD), $\langle (x(t) - x(0))^2 \rangle$, computed with MD, LE and GLE in the LDL and HDL cases. It is evident that both Markovian and non-Markovian coarse grainings are able to accurately reproduce the MSD. Moreover, in the HDL case, the GLE shows better performance with respect to the LE. Figures 11(c,d) depict the values of the adaptive learning rate η during the MLP learning process. The log-log plot highlights the wide range of η values spanning up to 8 orders of magnitude. This variability exemplifies the advantages of an adaptive learning rate over a fixed one. The cost function C evolution during the learning process is reported in Figs 11(e-f). The monotonically decreasing trend of C shows a plateau at some point which corresponds to the end of the learning process.

We now turn our attention to the performance of the adopted coarse-graining out of equilibrium by analyzing the PDF, ρ. A target particle with zero initial position x and momentum p is immersed in an equilibrated bath of 699 particles identical to the one adopted in the LDL case at equilibrium. 10^5 trajectories relaxing to equilibrium are simulated. This relaxation corresponds to the evolution of a Dirac delta to the equilibrium distribution in the phase space. Similarly, the relaxation of ρ obtained by coarse-graining the bath with both GLE and LE is followed. The comparison reported in Figs 12(a-f) shows that GLE, even if parameterized with a memory kernel evaluated at equilibrium conditions, significantly outperforms LE. As expected, at equilibrium the distributions obtained with MD, GLE and LE converge. During the relaxation, ρ relaxes faster for LE and GLE with respect to MD. A quantitative estimation of the accuracy of GLE in reproducing the density relaxation is provided by the mean square errors in position ϵ_q and momentum ϵ_p, shown in Figs 12(g,h). As expected, both errors are negligible at the start and asymptotically for large times when the system reaches equilibrium. During the initial stage of the relaxation, the errors ϵ_q and ϵ_p approach a peak, whose value for GLE is lower than that for LE by about 50% and 35%, respectively.

D Particle chain in a bath: simulation details

A chain of $N = 20$ colloidal particles in an LJ bath is also simulated, as shown in Fig. 13. For the multi-body Dreiding potential [30, 21], linear covalent bonds are approximated by the harmonic potential $v_H(\mathbf{r}_{ij}) = k_H(\mathbf{r}_{ij} - \mathbf{r}_0)^2$, where

Table 3: Results of the augmented ADF test for modified global temperature.

ADF Statistic:	-21.377945
p-value:	$< 10^{-16}$
lags:	54
Critical Values:	
1%:	-2.566
5%:	-1.941
10%:	-1.617

$\mathbf{r}_0$ is the equilibrium position and k_H is a positive constant. Similarly, angular covalent bonds are approximated by $v_\gamma(r_{ijk}) = k_\gamma(\gamma_{ijk} - \gamma_0)^2$, where γ_{ijk} is the angle in i formed by the particles i, j and k, γ_0 is the equilibrium angle and k_γ is a positive constant. Finally, we torsional (dihedral) bonds are modelled through the potential $v_\phi(r_{ijkl}) = k_\phi(1 + cos(2\phi_{ijkl}))$, with ϕ_{ijkl} being the angle between the two planes defined by $\{\mathbf{r}_i, \mathbf{r}_j, \mathbf{r}_k\}$ and $\{\mathbf{r}_j, \mathbf{r}_k, \mathbf{r}_l\}$ respectively, and k_ϕ being a positive parameter. Table 2 gives the values of all intermolecular parameters. The bath contains $69,900$ particles interacting with Lennard-Jones potential v_{LJ}. The simulation box measures $50 \times 50 \times 40$ in reduced units and periodic boundary conditions are imposed along the x, y and z axes. A Nosé-Hoover thermostat is used to equilibrate the system at a reduced temperature $T = 1.1$ with a time step $\Delta t = 10^{-2}$.

The following procedure is followed to run the MD simulations. First, the bath particles are randomly generated inside the simulation box. Then, the chain particles are placed along a straight line and a minimization algorithm is employed to avoid overlaps between them. Accordingly, a run of 1.5×10^5 time steps is used to equilibrate the system. Finally, data are gathered over 2×10^7 time steps.

GLE for time series

To model a general time series of an observable $\boldsymbol{\mathcal{O}}$ by means of a non-Markovian GLE the following conditions have to be satisfied:

- $\boldsymbol{\mathcal{O}}(t) \sim \mathcal{N}(\mu, \sigma^2)$,
- $\langle \boldsymbol{\mathcal{O}}(t) \rangle = 0 \quad \forall t$,
- $\langle \boldsymbol{\mathcal{O}}^2(t) \rangle = \sigma^2 \quad \forall t$,
- $\langle \boldsymbol{\mathcal{O}}(t)\boldsymbol{\mathcal{O}}(t') \rangle = \langle \boldsymbol{\mathcal{O}}(t-t')\boldsymbol{\mathcal{O}}(0) \rangle \quad \forall t \geq t'$.

If the original data of $\boldsymbol{\mathcal{O}}$ exhibits non-stationary features, some manipulation of the data is needed to obtain stationarity.

Case 1: Global temperature dynamics The yearly moving average is defined as:

$$T_y(t) = \frac{1}{y} \sum_{i=t-y-1}^{t-1} T(i). \tag{58}$$

To test the statistical properties ot T_a, we adopted the following tests. First, we employ the Q–Q (quantile-quantile) plot which compares two distributions by plotting their quantiles against each other. Quantiles are defined as sets of values of a stochastic variable splitting a distribution into an arbitrary number of intervals with identical probability. Figure 14(a) shows the QQ (quantile-quantile) plot which compares the data cumulative distribution against the normal theoretical cumulative distribution for each quantile. The red straight line represents the case in which the distribution of the data is exactly normal. Evidently, the time series data are well approximated by a normal distribution, especially in the theoretical quantile range $-3 < Q < 3$. Some tail effects are visible, but the overall agreement is quantitatively verified by the R-squared test which gives a value $R^2 = 0.9955$.

To test now the stationarity of mean variance, and time correlations, we split the data in 5 windows. Figure 14(b) shows that, assuming the observable of interest $T_a(t)$ is stationary, the maximum errors for the mean and standard deviation are 0.0183 and 0.0430, respectively. Moreover, as reported in Fig. 14(c), the maximum standard error between the time correlation for each window and their mean is 0.0246.

Finally, to test the stationarity of the modified time series, the augmented Dickey–Fuller (ADF) test is adopted. The est is useful to establish if a unit root is present in the stochastic data series. Specifically, the null hypothesis of a unit root is rejected in favor of the stationary alternative if the test statistic is more negative than some critical values. The results of ADF reported in Table 3 allows us to reject the unit root hypothesis with a probability higher than 99%.

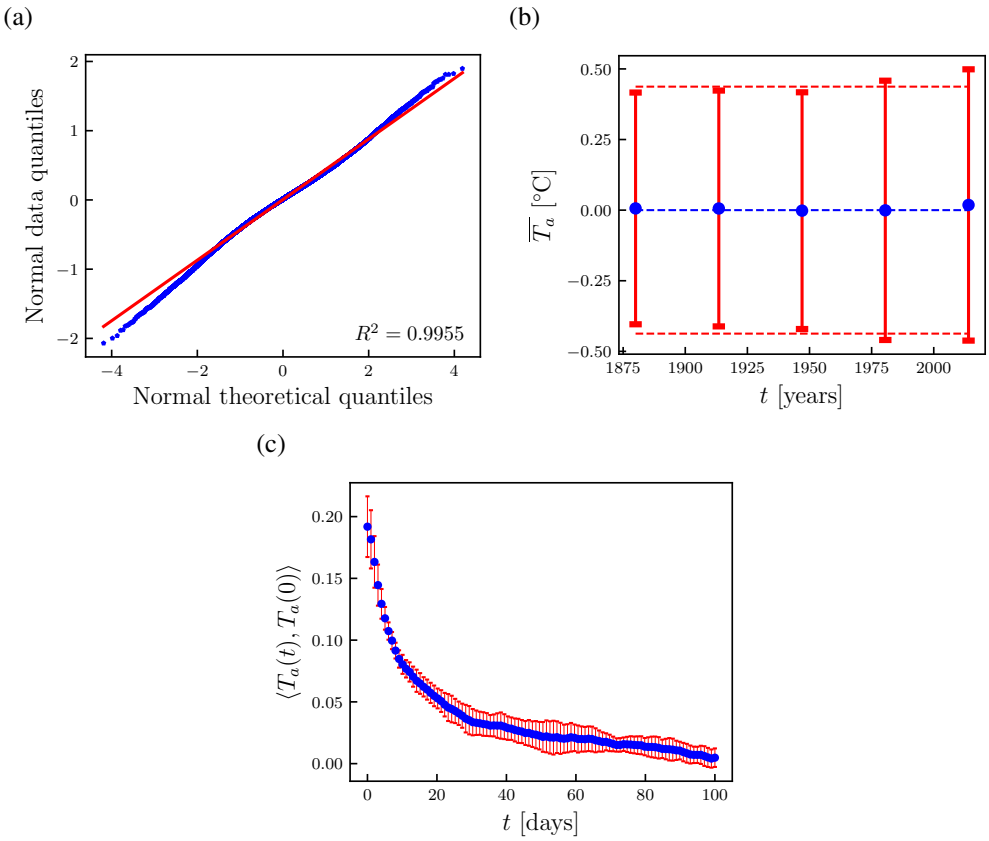

Figure 14: (a) QQ-plot for $T_a(t) = T(t) - T_y(t)$. The quantiles obtained from the distribution of the data are plotted against the quantiles computed directly from the normal distribution. (b) Mean of T_a evaluated for 5 different data windows in time (blue dots) and corresponding standard deviations represented as red error bars. (c) Average time correlation function (blue dots) and standard error evaluated at each time from the time correlations of 5 different data windows.

Table 4: Results of the augmented ADF test for modified Nikkei index.

ADF Statistic:	-29.805726
p-value:	$< 10^{-16}$
lags:	10
Critical Values:	
1%:	-2.566
5%:	-1.941
10%:	-1.617

Case 2: Nikkei index The moving average and the moving standard deviation are computed over a period $[t-y, t-1]$ as:

$$NI_y(t) = \frac{1}{y} \sum_{i=t-y-1}^{t-1} NI(i), \tag{59}$$

$$\sigma_y(t) = \sqrt{\frac{1}{y} \sum_{i=t-y-1}^{t-1} (NI(i) - NI_y(t))^2}. \tag{60}$$

The parameter y is appropriately chosen in order to obtain a stationary $NI_a(t)$; preliminary tests have shown that $y = 10$ days is an optimal value.

Figure 15(a) shows the QQ plot. The time series distribution is well approximated with a normal distribution in the theoretical quantile range $-2.5 < Q < 2.5$, but evidently, strong tail effects are present. This means that the Gaussian

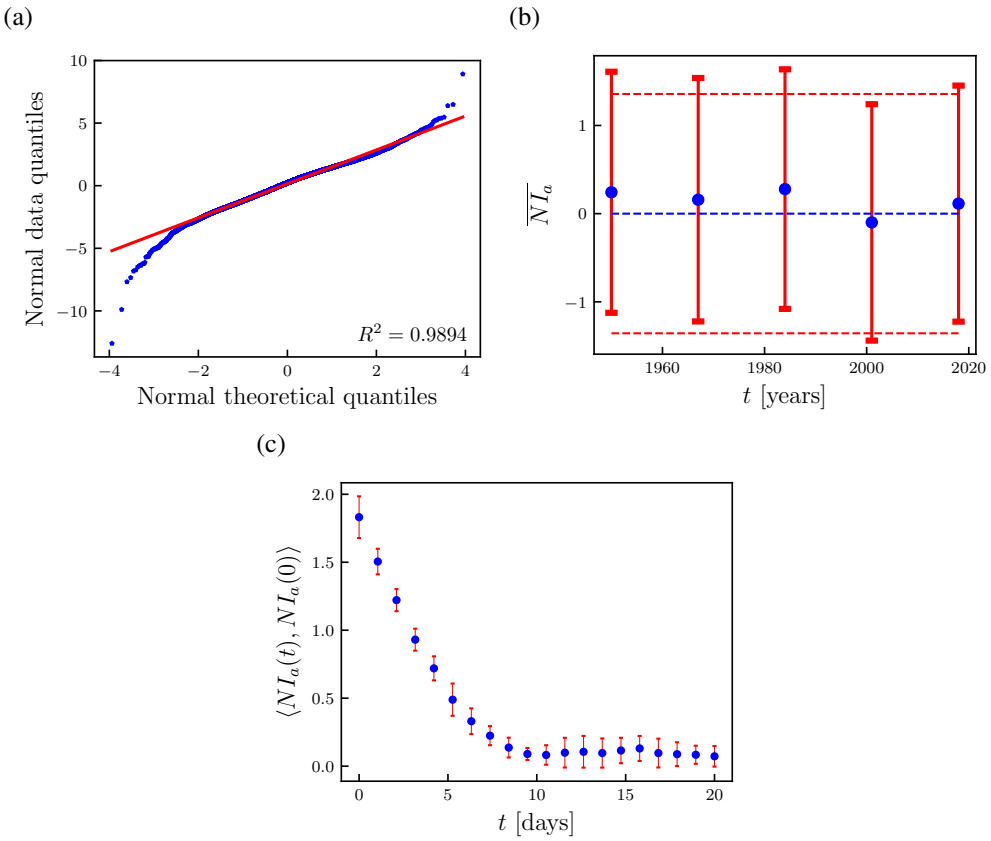

Figure 15: (a) QQ-plot for $NI_a(t) = NI(t) - NI_y(t)$. (b) Mean of NI_a evaluated for 5 different data windows in time (blue dots) and corresponding standard deviations represented as red error bars. (c) Average time correlation function (blue dots) and standard error evaluated at each time from the time correlations of 5 different data windows.

approximation, and consequently the GLE for $NI(t)$, remains valid as long as extreme market events, such as market crashes or crises, are avoided. The overall agreement is quantitatively verified by the R-squared test, which gives $R^2 = 0.9894$.

Finally, to test the stationarity of mean variance, and time correlations, we split the data in 5 equally sized sets and for each one we analyze their statistical properties. Figure 15(b) shows that, taking NI_a as the observable, the maximum errors for the mean and standard deviation are 0.2787 and 0.0234, respectively. But unlike the global temperature problem we considered earlier, the error for the mean is an order-of-magnitude higher, suggesting that stock markets are more challenging to model than natural phenomena. Moreover, as reported in Fig. 15(c), the maximum standard error between the time correlation in each window and their mean is 0.1082. The results of the ADF test reported in Table 4 allow us to reject the unit root hypothesis with a probability higher than 99%.

Acknowledgment

We acknowledge financial support from the Imperial College Chemical Engineering PhD Scholarship scheme, European Research Council via Advanced Grant No. 247031, Engineering and Physical Sciences Research Council of the UK via grants No. EP/L025159 and EP/L020564 and the Defense Advanced Research Projects Agency of the USA.

References

[1] Peter Alaton, Boualem Djehiche, and David Stillberger. On modeling and pricing weather derivatives. *Appl. Math. Fin.*, 9(1):1–20, 02 2002.

[2] A. D. Baczewski and S. D. Bond. Numerical integration of the extended variable generalized Langevin equation with a positive Prony representable memory kernel. *J. Chem. Phys.*, 139(4):044107, 2013.

[3] Berkeley-Earth. Experimental land-average temperature for period 1880–2014. http://berkeleyearth.lbl.gov/auto/Global/Complete_TAVG_daily.txt, 2018.

[4] Marvin Bishop, M. H. Kalos, and H. L. Frisch. Molecular dynamics of polymeric systems. *J. Chem. Phys.*, 70(3):1299–1304, 1979.

[5] Minxin Chen, Xiaotao Li, and Chun Liu. Computation of the memory functions in the generalized Langevin models for collective dynamics of macromolecules. *J. Chem. Phys.*, 141(6):064112, 2014.

[6] A. J. Chorin, O. H. Hald, and R. Kupferman. Optimal prediction and the Mori–Zwanzig representation of irreversible processes. *PNAS*, 97(7):2968–2973, 2000.

[7] Alexandre Chorin and Panagiotis Stinis. Problem reduction, renormalization, and memory. *Commun. Appl. Math. Comput. Sci.*, 1(1):1–27, 2006.

[8] Eric Darve, Jose Solomon, and Amirali Kia. Computing generalized Langevin equations and generalized Fokker–Planck equations. *PNAS*, 106(27):10884–10889, 2009.

[9] D. I. Dimitrov, A. Milchev, Kurt Binder, Leonid I. Klushin, and Alexander M. Skvortsov. Universal properties of a single polymer chain in slit: Scaling versus molecular dynamics simulations. *J. Chem. Phys.*, 128(23):234902, 2008.

[10] M. A. Durán-Olivencia, P. Yatsyshin, B. D. Goddard, and S. Kalliadasis. General framework for fluctuating dynamic density functional theory. *New J. Phys.*, 19:123022, 2017.

[11] Andrew L. Ferguson, Athanassios Z. Panagiotopoulos, Pablo G. Debenedetti, and Ioannis G. Kevrekidis. Systematic determination of order parameters for chain dynamics using diffusion maps. *PNAS*, 107(31):13597–13602, 2010.

[12] E. Friis-Christensen and K. Lasses. Length of the solar cycle: An indicator of solar activity closely associated with climate. *Science*, 254(5032):698–700, 1991.

[13] Dror Givon, Raz Kupferman, and Andrew Stuart. Extracting macroscopic dynamics: model problems and algorithms. *Nonlinearity*, 17(6):R55, 2004.

[14] Benjamin D. Goddard, Andreas Nold, Nikos Savva, Grigorios A. Pavliotis, and Serafim Kalliadasis. General dynamical density functional theory for classical fluids. *Phys. Rev. Lett.*, 109:120603, 2012.

[15] Georg A. Gottwald, Daan T. Crommelin, and Christian L. E. Franzke. *Stochastic Climate Theory*, pages 209–240. Cambridge University Press, 2017.

[16] H Grabert. *Projection Operator Techniques in Nonequilibrium Statistical Mechanics*. Springer-Verlag Berlin Heidelberg, 1982.

[17] Carmen Hijón, Pep Español, Eric Vanden-Eijnden, and Rafael Delgado-Buscalioni. Mori–Zwanzig formalism as a practical computational tool. *Faraday Discuss.*, 144:301–322, 2010.

[18] Sepp Hochreiter and Jurgen Schmidhuber. Long short-term memory. *Neural Computation*, 9(8):1735–1780, 1997.

[19] Kurt Hornik. Approximation capabilities of multilayer feedforward networks. *Neural Netw.*, 4(2):251–257, 1991.

[20] Kurt Hornik, Maxwell Stinchcombe, and Halbert White. Multilayer feedforward networks are universal approximators. *Neural Netw.*, 2(5):359–366, 1989.

[21] D. Hossain, M.A. Tschopp, D.K. Ward, J.L. Bouvard, P. Wang, and M.F. Horstemeyer. Molecular dynamics simulations of deformation mechanisms of amorphous polyethylene. *Polymer*, 51(25):6071 – 6083, 2010.

[22] Shinnosuke Kawai. On the environmental modes for the generalized Langevin equation. *J. Chem. Phys.*, 143(9):094101, 2015.

[23] Tomoyuki Kinjo and Shiaki Hyodo. Equation of motion for coarse-grained simulation based on microscopic description. *Phys. Rev. E*, 75:051109, May 2007.

[24] Ilan Koren and Graham Feingold. Aerosol-cloud-precipitation system as a predator-prey problem. *PNAS*, 108:12227–12232, 2011.

[25] Oliver F. Lange and Helmut Grubmüller. Collective Langevin dynamics of conformational motions in proteins. *J. Chem. Phys.*, 124(21):214903, 2006.

[26] Min G. Lee, Akihiko Oba, and Hideki Takayasu. *Parameter Estimation of a Generalized Langevin Equation of Market Price*, pages 260–270. Springer Japan, Tokyo, 2002.

[27] Huan Lei, Nathan A. Baker, and Xiantao Li. Data-driven parameterization of the generalized Langevin equation. *PNAS*, 113(50):14183–14188, 2016.

[28] Don S. Lemons and Anthony Gythiel. Paul Langevin's 1908 paper "On the Theory of Brownian Motion"["Sur la théorie du mouvement brownien," C. R. Acad. Sci. (Paris) 146, 530-533 (1908)]. *American Journal of Physics*, 65(11):1079–1081, 1997.

[29] macrotrends.net. Nikkei 225 index - 67 year historical chart. www.macrotrends.net/2593/nikkei-225-index-historical-chart-data, 2018.

[30] Stephen L. Mayo, Barry D. Olafson, and William A. Goddard. Dreiding: a generic force field for molecular simulations. *J. Phys. Chem.*, 94(26):8897–8909, 1990.

[31] E. Moreles and D. Martínez-López. Analysis of the simulated global temperature using a simple energy balance stochastic model. *Atmósfera*, 29(4):279–297, 2016.

[32] Hazime Mori. Transport, collective motion, and brownian motion. *Prog. Theor. Phys.*, 33(3):423–455, 1965.

[33] M. A. Nielsen. *Neural Networks and Deep Learning*. Determination Press, 2015.

[34] Martin Riedmiller. Advanced supervised learning in multi-layer perceptrons– from backpropagation to adaptive learning algorithms. *Comp. Stand. Inter.*, 16(3):265–278, 1994.

[35] Robert Rohde, Richard Muller, Robert Jacobsen, Saul Perlmutter, Arthur Rosenfeld, Jonathan Wurtele, Judith Curry, Charlotte Wickham, and Steven Mosher. Berkeley earth temperature averaging process. *Geoinfor. Geostat.: An Overview*, 1(2), 2013.

[36] Amit Singer, Radek Erban, Ioannis G. Kevrekidis, and Ronald R. Coifman. Detecting intrinsic slow variables in stochastic dynamical systems by anisotropic diffusion maps. *PNAS*, 106(38):16090–16095, 2009.

[37] Masafumi Takahashi. Non-ideal brownian motion, generalized Langevin equation and its application to the security market. *Fin. Eng. Japanese Markets*, 3(2):87–119, Jul 1996.

[38] Sean J. Taylor and Benjamin Lethamn. Forecasting at scale. *PeerJPreprint*, 2017.

[39] Alexis Torres-Carbajal, Salvador Herrera-Velarde, and Ramón Castañeda Priego. Brownian motion of a nano-colloidal particle: the role of the solvent. *Phys. Chem. Chem. Phys.*, 17:19557–19568, 2015.

[40] Robert Zwanzig. Ensemble method in the theory of irreversibility. *J. Chem. Phys.*, 33(5):1338–1341, 1960.

[41] Robert Zwanzig. Nonlinear generalized Langevin equations. *J. Stat. Phys.*, 9(3):215–220, 1973.

[42] Robert Zwanzig. *Nonequilibrium Statistical Mechanics*. Oxford University Press, 2001.